

Motion2VecSets: 4D Latent Vector Set Diffusion for Non-rigid Shape Reconstruction and Tracking

Wei Cao^{1*} Chang Luo^{1*} Biao Zhang² Matthias Nießner¹ Jiapeng Tang¹

¹Technical University of Munich ²KAUST

<https://vveicao.github.io/projects/Motion2VecSets/>

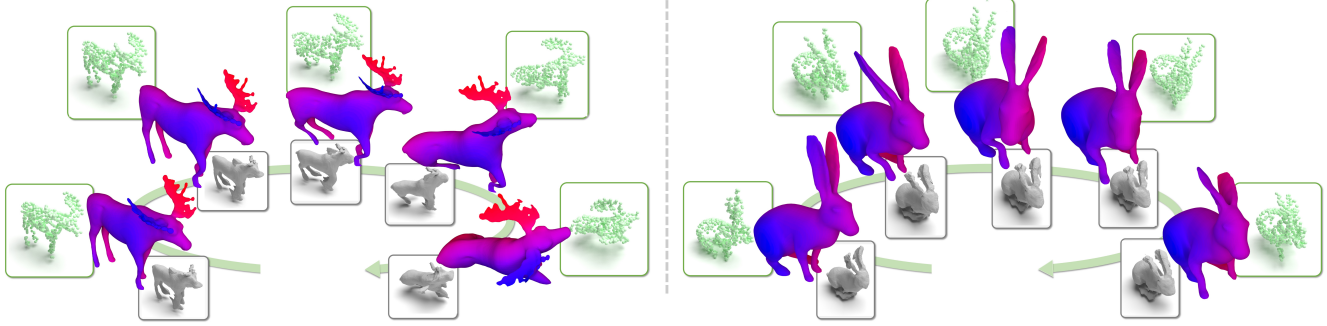


Figure 1. We present **Motion2VecSets**, a 4D diffusion model for dynamic surface reconstruction from sparse, noisy, or partial **point cloud sequences**. Compared to the existing state-of-the-art method **CaDeX** [26], our method can reconstruct more plausible non-rigid object surfaces with complicated structures and achieve more robust motion tracking.

Abstract

We introduce *Motion2VecSets*, a 4D diffusion model for dynamic surface reconstruction from point cloud sequences. While existing state-of-the-art methods have demonstrated success in reconstructing non-rigid objects using neural field representations, conventional feed-forward networks encounter challenges with ambiguous observations from noisy, partial, or sparse point clouds. To address these challenges, we introduce a diffusion model that explicitly learns the shape and motion distribution of non-rigid objects through an iterative denoising process of compressed latent representations. The diffusion-based prior enables more plausible and probabilistic reconstructions when handling ambiguous inputs. We parameterize 4D dynamics with latent vector sets instead of using a global latent. This novel 4D representation allows us to learn local surface shape and deformation patterns, leading to more accurate non-linear motion capture and significantly improving generalizability to unseen motions and identities. For more temporal-coherent object tracking, we synchronously denoise deformation latent sets and exchange information across multiple frames. To avoid the computational over-

head, we design an interleaved space and time attention block to alternately aggregate deformation latents along spatial and temporal domains. Extensive comparisons against the state-of-the-art methods demonstrate the superiority of our *Motion2VecSets* in 4D reconstruction from various imperfect observations, notably achieving a 19% improvement in Intersection over Union (IoU) compared to *CaDeX* [26] for reconstructing unseen individuals from sparse point clouds on the *DeformingThings4D-Animals* dataset [29].

1. Introduction

Our world, dynamic in its 4D nature, demands an increasingly sophisticated understanding and simulation of our living environment. This offers significant potential for practical applications, including Virtual Reality (VR), Augmented Reality (AR), and robotic simulations.

There have been notable advancements in 3D object modeling, particularly in representations through parametric models [28, 31, 37, 46, 65]. Unfortunately, these template-based models are not suitable to effectively capture the 4D dynamics of general non-rigid objects, due to the assumption of a fixed template mesh. The model-free

* Equal Contribution.

approaches [26, 33, 52] represent a significant advancement by using coordinate-MLP representations for deformable object reconstruction with arbitrary topologies and non-unified structures. However, these state-of-the-art methods still encounter challenges when facing ambiguous observations of noisy, sparse, or partial point clouds since it is an ill-posed problem where multiple possible reconstructions can match with the input. Besides, they represent dynamics as a sequence of single latent codes and thus struggle to capture shape and motion priors accurately. These issues become even more severe with unseen identities, due to the limited generalizability of global latent representation.

To address above mentioned challenges, we propose Motion2VecSets, a diffusion model designed for 4D dynamic surface reconstruction from sparse, noisy, or partial point clouds. It explicitly learns the joint distribution of non-rigid object surfaces and temporal dynamics through an iterative denoising process of compressed latent representations. This enables more realistic and varied reconstructions, particularly when dealing with ambiguous inputs. Inspired by the observation that objects with varying topologies often share similar local geometry and deformation patterns, we represent dynamic surfaces as a sequence of latent vector sets to preserve local shape and deformation details. One for shape modeling of the initial frame and others to describe the temporal evolution from the initial frame. This latent vector set representation naturally enables the learning of more accurate shape and motion priors, enhancing the model’s generalization capacity to unseen identities and motions. Specifically, we introduce Synchronized Deformation Vector Set Diffusion, which simultaneously denoises the deformation latent sets across different time frames to enforce spatio-temporal consistency over dynamic surfaces. To manage the memory consumption associated with multiple deformation latent set diffusions, we design interleaved space and time attention block as the basic unit for the denoiser. These blocks aggregate deformation latent sets along spatial and temporal domains in an alternating manner. As illustrated in Figure 1, our Motion2VecSets can reconstruct more plausible non-rigid object surfaces with complicated structures and achieve more robust motion tracking than the existing state-of-the-art. Our contributions can be summarized as follows:

- We present a 4D latent diffusion model designed for dynamic surface reconstruction, adept at handling sparse, partial, and noisy point clouds.
- We introduce a 4D neural representation with latent vector sets, significantly enhancing the capacity to represent complicated shapes as well as motions and improving generalizability to unseen identities and motions.
- We design an Interleaved Spatio-Temporal Attention mechanism for synchronized diffusion of deformation latent sets, achieving robust spatio-temporal consistency

and advanced computational efficiency.

Extensive comparisons against the state-of-the-art methods demonstrate the superiority of our Motion2VecSets in dynamic surface reconstruction on the Dynamic FAUST [4] and the DeformingThings4D-Animals [29] datasets.

2. Related works

3D Shapes Traditional methods in 3D representation have primarily employed meshes [19, 30, 39, 49, 50, 59], point clouds [1, 16, 63], and voxels [13, 17, 20, 44, 48] to depict geometry. Complementing these are parametric models, which have effectively represented specific shape categories, such as human bodies (e.g., SMPL [31], STAR [37]), faces (e.g., FLAME [28]), hands (e.g., MANO [46]), and animals (e.g., SMAL [65]). However, these parametric approaches often rely on fixed template topologies, which can lead to difficulties in accurately modeling general non-rigid objects without consistent topological structures. Meanwhile, recent advancements in 3D representation are increasingly adopting implicit methods [6, 7, 10, 11, 18, 33, 40, 51, 58, 61], known for their greater flexibility to represent objects with arbitrary topologies. Notably, Occupancy Networks [33] and DeepSDF [40] employ a continuous implicit framework, enabling the representation of volumetric grids with potentially infinite resolution.

4D Dynamics Recent advancements have successfully extended 3D representations to 4D, which captures object dynamics more effectively [5, 16, 24, 26, 27, 36, 38, 52, 54]. For instance, OFlow [36] incorporates Neural-ODE [56] to simulate deformations. LPDC [52] replaces Neural-ODE with an MLP and learns local spatio-temporal codes, capturing both shape and deformations. CaDeX [26] employs a learnable deformation embedding between each frame and its canonical shape. Despite these advancements, methods relying on either ODE [36] solvers or a single global latent vector [26, 38, 52] coupled with an MLP network face challenges in accurately capturing complex real-world 4D dynamics, particularly in non-rigid objects. Drawing inspiration from 3DShape2Vecset [61], which uses a set of latent codes to represent similar local geometry patterns across objects, our proposed method leverages a similar approach to characterize 4D dynamics. Different objects share similar local deformation patterns, our framework uniquely assigns a distinct learnable latent code to each local region, significantly enhancing its ability to precisely model and generalize to unseen identities and motions.

Diffusion Models Diffusion models [21], known for their Markov chain-based denoising capability, have gained impressive progress in multiple domains, including image and

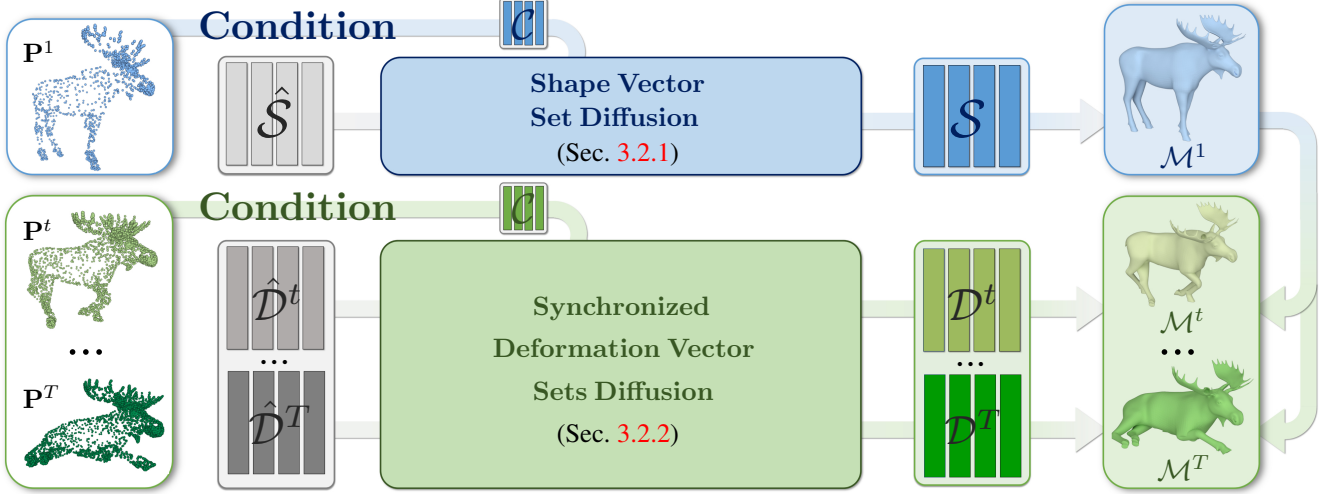


Figure 2. **Overview Pipeline of Motion2VecSets.** Given a sequence of sparse and noisy point clouds as inputs $\{\mathbf{P}^t\}_{t=1}^T$, Motion2VecSets outputs a continuous mesh sequence $\{\mathcal{M}^t\}_{t=1}^T$. The initial input frame \mathbf{P}^1 (top left) is used as condition in the **Shape Vector Set Diffusion** (Sec. 3.2.1), yielding denoised shape codes \mathcal{S} for reconstructing the geometry of the reference frame \mathcal{M}^1 (top right). Concurrently, the subsequent input frames $\{\mathbf{P}^t\}_{t=2}^T$ (bottom left) are utilized in the **Synchronized Deformation Vector Sets Diffusion** to produce denoised deformation codes $\{\mathcal{D}^t\}_{t=2}^T$, where each latent set \mathcal{D}^t encodes the deformation from the reference frame \mathcal{M}^1 to each subsequent frame \mathcal{M}^t .

video processing [8, 15, 22, 34, 35], 3D vision [3, 12, 23, 32, 45, 53, 55, 57]. These models are adept at capturing complex data distributions. In the field of 3D vision, their applications are varied: Luo et al. [32] have successfully applied diffusion models to point cloud generation, and Rombach *et al.* [3, 45] have adapted them for latent space representations. Additionally, integration with PointNet [42] and triplane features [41], as seen in DiffusionSDF [12], has further enhanced their training capabilities. Concurrent work NAP [27] advances 3D object generation by effectively modeling articulated objects with a novel parameterization and diffusion-denoising approach. A key challenge in representing 4D dynamics with existing diffusion models is their tendency to adapt 3D models directly to 4D and process each frame independently, which can result in discontinuities in temporal and spatial relationships. To bridge this gap, our approach implements a synchronous denoising process for sets of codes. This innovation ensures not only a reduction in spatial complexity but also consistent deformations in latent space. Moreover, recent works [14, 23, 43, 47, 57, 60, 62] in the field of 3D pose estimation and generation also indicate the power of diffusion models. DiffPose [23] utilizes the diffusion model to handle very ambiguous poses and can even predict an infinite number of poses. PhysDiff [60] produces physically plausible motions by incorporating a physics-based motion projection within its diffusion process. However, These methods are still in the realm of pose, our method expands the application of diffusion models to a broader range of deformable surfaces of general non-rigid objects.

3. Approach

The inputs are T frames of sparse or partial noisy point clouds, represented by $\mathcal{P} = \{\mathbf{P}^t\}_{t=1}^T$, where $\mathbf{P}^t = \{\mathbf{p}_i \in \mathbb{R}^3\}_{i=1}^L$, L represents the number of points. The goal is to reconstruct continuous 3D meshes with high fidelity, denoted as $\{\mathcal{M}^t\}_{t=1}^T = \{\mathcal{V}^t, \mathcal{F}^t\}_{t=1}^T$, where \mathcal{V}^t and \mathcal{F}^t refer to the set of vertices faces of the reconstructed mesh at time frame t . Conventional feed-forward models face challenges in handling ambiguous inputs within an ill-posed problem setting. Particularly, when observations are sparse, partial, and noisy, generating meaningful reconstructions becomes highly challenging without robust prior knowledge. To reconstruct high-fidelity dynamic shapes accurately, we proposed 4D latent set diffusion to learn shape and motion priors, explicitly learning the distribution of deformable object surface sequences via compressed latent vector sets. While the diffusion model enhances realistic surface reconstruction and deformation tracking, generating multi-modal outputs, the latent set representation and transformer architecture provide the capability to capture more accurate geometry and deformation priors.

3.1. 4D Neural Representation with Latent Sets

Previous works often utilize single global codes [26, 36, 52] to represent 4D sequences, potentially losing significant surface geometry and temporal evolution information. To retain as much detail as possible, we advocate the use of two distinct sets of latent vectors. Specifically, the *shape latent set* is responsible for reconstructing the initial frame,

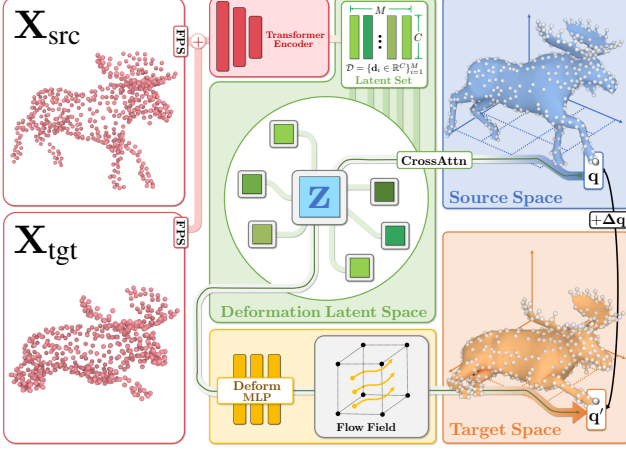


Figure 3. **Deformation Autoencoder.** Given a pair of point clouds \mathbf{X}_{src} and \mathbf{X}_{tgt} from two frames of a dynamic mesh sequence, we initially downsample them using farthest point sampling (FPS). Subsequently, the concatenated points are passed into **transformer encoder** to generate the **Deformation Latent Set** \mathcal{D} . For a query point \mathbf{q} in the source space, a cross-attention layer is utilized to match the most relevant **fused feature** \mathbf{z} . This selected feature is subsequently fed into the **deformation MLP decoder** to predict an offset $\Delta \mathbf{q}$, translating it to \mathbf{q}' in the target space. To reduce the feature diversity of \mathcal{D} , KL-regularization is employed.

serving as the reference frame, while the deformation correspondences between the reference and subsequent frames are encoded by the *deformation latent set*. Compared to previous methods [26, 36, 52] relying on a single global code, we assign local latent codes to individual local regions, which significantly improve the network’s capability to accurately model non-linear motions and generalize to unseen identities and motions. Given the fact that different non-rigid objects share similar local geometry and deformation patterns, the latent sets can also increase the generalization ability to handle unseen motions and identities.

Shape Latent Set Similar to 3DShape2VecSet [61], we utilize a shape autoencoder to compress the surface of the initial frame into a set of latent codes. Concretely, we leverage a transformer encoder to condense the 3D surface of the initial frame into a set of latent vectors denoted as $\mathcal{S} = \{\mathbf{s}_i \in \mathbb{R}^C\}_{i=1}^M$. Here, M represents the overall count of codes and C denotes their dimensionality. Following that, a cross-attention layer is used to fuse the latent codes for occupancy field prediction through an MLP. Training is processed by minimizing the binary cross-entropy (BCE) loss, which aligns the predicted occupancy $\hat{\mathcal{O}}(\mathcal{Q})$ with the actual occupancy $\mathcal{O}(\mathcal{Q})$, \mathcal{Q} refers to the query points:

$$\mathcal{L}_{\text{recon}}(\mathcal{S}, \mathcal{Q}) = \mathbb{E}_{\mathcal{Q} \in \mathbb{R}^3} [\text{BCE}(\hat{\mathcal{O}}, \mathcal{O})] \quad (1)$$

Deformation Latent Set As shown in Figure 3, to represent the deformation between different non-rigid poses, we first sample a pair of point clouds \mathbf{X}_{src} and \mathbf{X}_{tgt} of size N with same sampling indices from a mesh sequence. Then, we employ a uniform farthest point sampling (FPS) strategy to eliminate spatial redundancy while preserving point correspondence. This process facilitates a concatenation step, where we combine the original and downsampled pairs of point clouds $\{\mathbf{X}_{\text{src}}, \mathbf{X}_{\text{tgt}}\}$, respectively. The subsequent transformer encoder is applied to extract deformation details in the local regions around subsampled points, resulting in the deformation latent set denoted as $\mathcal{D} = \{\mathbf{d}_i \in \mathbb{R}^C\}_{i=1}^M$. Query point $\mathbf{q} \in \mathcal{Q}_{\text{src}}$ from the source space is utilized as the query for cross-attention, extracting the most relevant fused feature \mathbf{z} in the deformation latent space. A linear deformation layer then maps these features to the predicted target points \mathbf{q}' through a flow field. The correspondence loss calculates the ℓ_2 -norm distance between the predicted and true target point clouds:

$$\mathcal{L}_{\text{corr}}(\mathcal{D}, \mathcal{Q}_{\text{src}}) = \mathbb{E}_{\mathcal{Q}_{\text{src}} \in \mathbb{R}^3} [\text{MSE}(\hat{\mathcal{Q}}_{\text{tgt}}, \mathcal{Q}_{\text{tgt}})] \quad (2)$$

KL Regularization Consistent with the latent diffusion framework [45], our model incorporates KL-regularization in the latent space to modulate feature diversity. This ensures the preservation of high-level features and keeps coherent global geometric and deformation patterns, which promotes the learning of diffusion models.

In summary, we characterize a sequence through the shape latent set \mathcal{S}^1 of the initial reference frame, which describes the implicit surface, and deformation latent sets $\mathcal{D}^2, \mathcal{D}^3, \dots, \mathcal{D}^T$ that depict the dense correspondences between the initial reference frame and the subsequent frames.

3.2. 4D Latent Vector Set Diffusion

3.2.1 Shape Diffusion

Following the diffusion paradigm in EDM by Karras et al. [25], we aim to minimize the expected ℓ_2 -denoising error. This is achieved by adding the noise ϵ sampled from the Gaussian distribution to the shape latent set \mathcal{S} , and then feeding the noise-added code $\hat{\mathcal{S}} = \mathcal{S} + \epsilon$ to the denoiser (to avoid confusing, we also use \mathcal{S} to represent its matrix form $\mathbb{R}^{N \times C}$). The whole process is denoted as:

$$\mathbb{E}_{\epsilon \sim \mathcal{N}(0, \sigma^2 \mathbf{I})} \left\| \text{Denoiser}(\hat{\mathcal{S}}, \sigma, \mathcal{C}) - \mathcal{S} \right\|_2^2 \quad (3)$$

Here, σ represents the noise level. Conditional latent set \mathcal{C} is defined as $\mathcal{C}(\mathbf{P}^1) = \{c_i \in \mathbb{R}^C\}_{i=1}^M$, which is generated by sending the first input frame \mathbf{P}^1 to the conditional encoder.

3.2.2 Synchronized Deformation Diffusion

To adapt those 3D models [28, 37, 46, 65] directly to 4D, the most straightforward approach is frame-by-frame process-

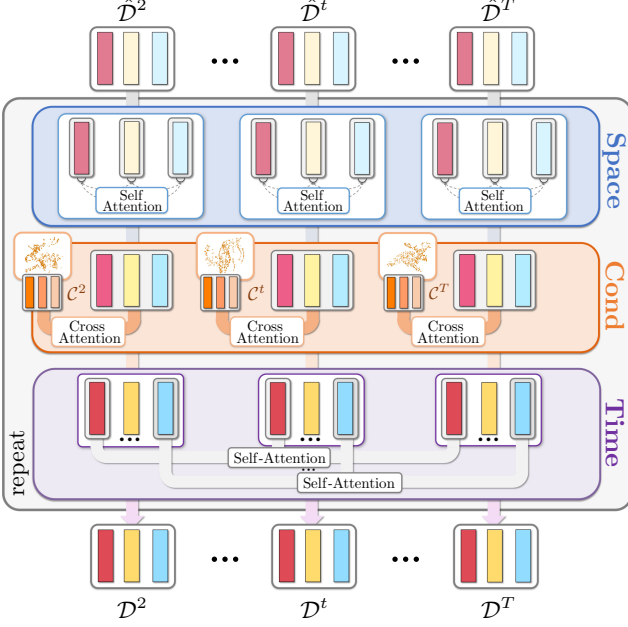


Figure 4. **Synchronized Deformation Vector Set Diffusion.** Given noised deformation vector sets $\{\hat{\mathcal{D}}^t\}_{t=1}^T$ (top) from a sequence, each set denoted as $\hat{\mathcal{D}}^t = \{\hat{\mathbf{d}}_1^t, \dots, \hat{\mathbf{d}}_M^t\}$ of timestep $t \in [2, T]$, we use repeated Interleaved Spatio-Temporal Attention Blocks (ISTA) as our denoising network. In each ISTA block, we first pass them to the space self-attention layer (*Space Attention*) to aggregate latent features $\hat{\mathcal{D}}^t$ across different spatial locations within each frame to explore spatial contexts. Next, we inject conditional information extracted from sparse or partial point clouds via cross-attention (*Condition Attention*) between conditional codes \mathcal{C}^t and noised deformation codes $\hat{\mathcal{D}}^t$ at each frame. Lastly, to enhance temporal coherence, a time self-attention layer (*Time Attention*) is used to aggregate latent codes from the same position but from different frames, i.e. $\{\hat{\mathbf{d}}_i^t\}_{t=2}^T$. Repeat this ISTA block and we finally get denoised deformation latent sets $\{\mathcal{D}^t\}_{t=2}^T$ (bottom).

ing, which may lead to potential discontinuities in temporal and spatial correspondence. Another approach is to aggregate all spatial-temporal point clouds, which would significantly increase the time complexity to $O(T^2N^2)$ for a sequence of T frames and N points each. However, our 4D latent set representation allows us to bypass the need for brute-force attention across spatial and temporal domains. As discussed in Sec. 3.1, the deformation latents at identical spatial positions across different frames correspond to the deformation behaviors of the same local surface region. Leveraging this property, we implement an alternating aggregation approach for the latent features, systematically switching between the spatial and temporal domains. This method not only enhances efficiency but also preserves the accuracy of our model, leading to a reduction in time complexity to $O(TN^2)$ in the spatial domain and $O(NT^2)$ in the temporal domain.

The details of synchronized deformation diffusion are described as follows. Given sparse input point clouds $\mathcal{P} = \{\mathbf{P}^t\}_{t=1}^T$, we pair subsequent frames with the first reference frame \mathbf{P}^1 , i.e., $\{\mathbf{P}^1, \mathbf{P}^t\}_{t=2}^T$. These pairs are encoded into a series of conditional latents $\mathcal{C}^t(\mathbf{P}^1, \mathbf{P}^t) = \{\mathbf{c}_i \in \mathbb{R}^C\}_{i=1}^M$ via a transformer encoder. Subsequently, these conditional latents, together with the diffused shape latent set \mathcal{S}^1 in Sec. 3.2.1, are injected into the denoising network as the condition, which provides useful guidance for the network to handle ambiguous scenarios, such as partial observation.

Interleaved Spatio-Temporal Attention Figure 4 depicts the denoiser network of our proposed synchronized deformation latent set diffusion. The basic unit is the designed Interleave Spatio-temporal Attention Block (ISTA). Each ISTA block contains three attention layers: *Space Self-Attention Layer*, *Conditional Cross-Attention Layer* and *Time Self-Attention Layer*. The *Space Self-Attention Layer* initiates spatial information exchange within each set of noised deformation codes $\hat{\mathcal{D}}^t = \{\hat{\mathbf{d}}_i^t\}_{i=1}^M$:

$$\text{SpaceAttn} = \text{SelfAttn}(\{\hat{\mathbf{d}}_i^t\}_{i=1}^M) \quad (4)$$

This is then followed by the *Conditional Cross-Attention Layer*. Conditional codes $\mathcal{C}^t(\mathbf{P}^1, \mathbf{P}^t) = \{\mathbf{c}_i \in \mathbb{R}^C\}_{i=1}^M$ from a partial or sparse point cloud are subjected to cross-attention with **CondAttn**:

$$\text{CondAttn} = \text{CrossAttn}(\{\hat{\mathbf{d}}_i^t\}_{i=1}^M, \mathcal{C}^t) \quad (5)$$

Finally, to improve coherence in the time dimension, a *Time Self-Attention Layer* is implemented among deformation codes from different timesteps but from the same position (same index i but different t). Consequently, through this setup, the **TimeAttn** is effectively obtained:

$$\text{TimeAttn} = \text{SelfAttn}(\{\hat{\mathbf{d}}_i^t\}_{t=2}^T) \quad (6)$$

In the denoising phase, we regard the entire sequence of deformation codes as a unified entity and apply a uniform noise reduction strategy across all codes, which preserves the consistency of local deformation patterns. Contrary to assigning individual noise to each set of shape codes, we add a consistent uniform noise ϵ to the deformation codes of the entire sequence $\{\hat{\mathcal{D}}^t\}_{t=2}^T = \{\mathcal{D}^t\}_{t=2}^T + \epsilon$. The denoising objective is thus formulated as:

$$\mathbb{E}_{\epsilon \sim \mathcal{N}(0, \sigma^2 \mathbf{I})} \left\| \text{Denoiser} \left(\{\hat{\mathcal{D}}^t\}_{t=2}^T, \sigma, \mathcal{C} \right) - \{\mathcal{D}^t\}_{t=2}^T \right\|_2^2 \quad (7)$$

Here, \mathcal{C} represents conditional codes derived from observations, $\{\mathcal{D}^t\}_{t=2}^T$ can also be represented in its 3D matrix form as $\mathbb{R}^{M \times (T-1) \times C}$. This approach not only ensures uniformity in the denoising process but also significantly reduces computational overhead.

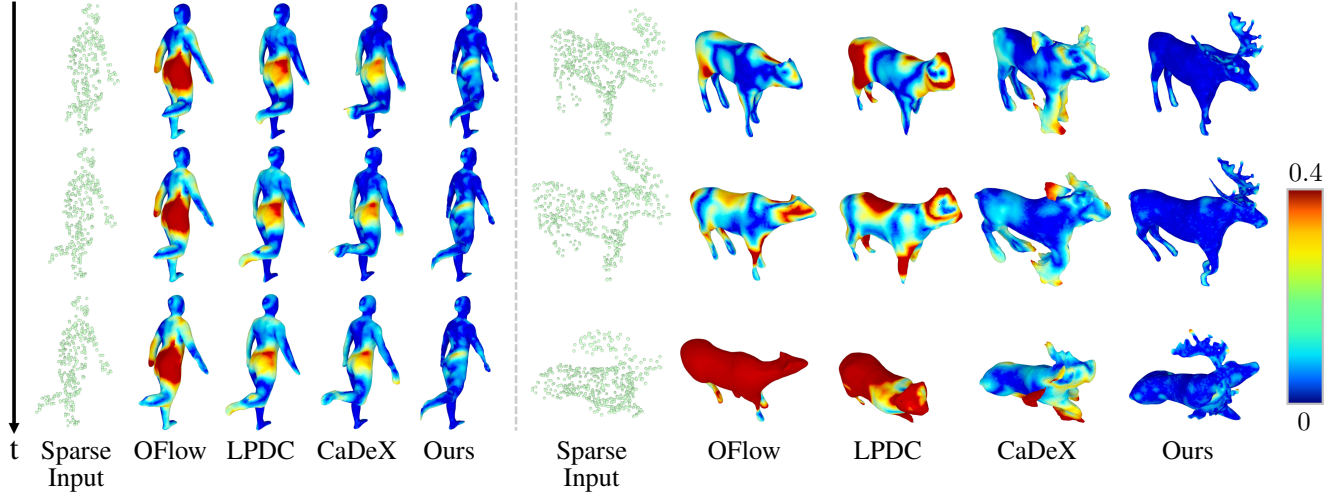


Figure 5. Comparisons of 4D Shape Reconstruction from **sparse and noisy** point clouds on the D-FAUST [4] (left) and the DT4D-A [29] (right) datasets. We visualize the Chamfer Distance between reconstruction and ground-truths as error maps. Our method can reconstruct more accurate surface geometries and motion dynamics.

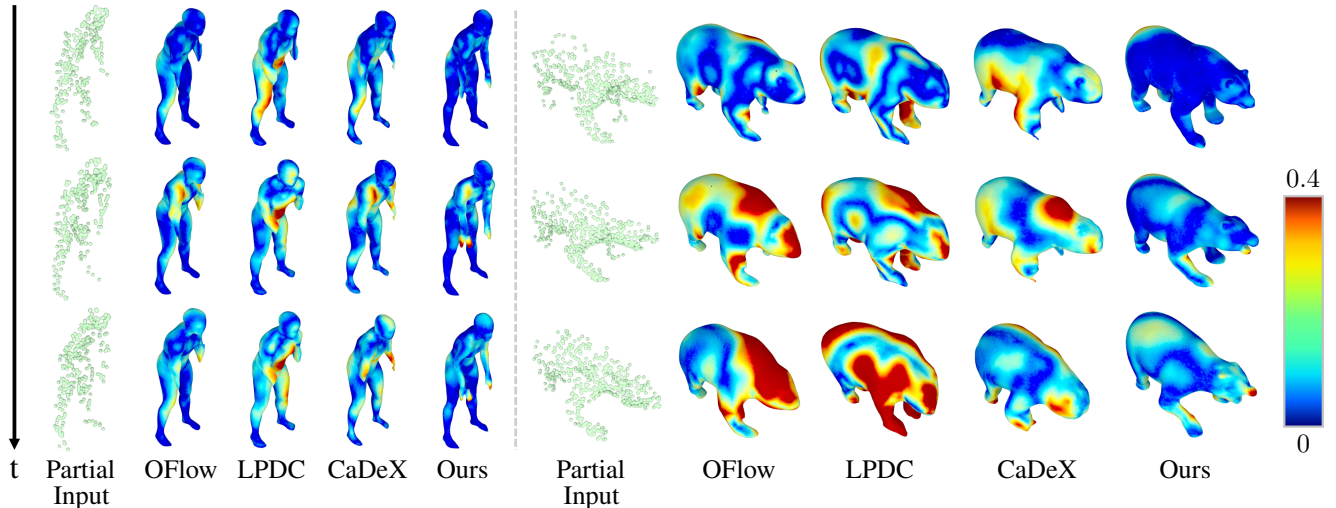


Figure 6. Comparisons of 4D Shape Completion from **monocular noisy depth scans** on D-FAUST [4] (left) and DT4D-A [29] (right) datasets. Our method exhibits lower reconstruction errors and achieves more plausible tracking.

4. Experiments

Datasets: To validate our model, we conducted experiments with two datasets. The first, Dynamic FAUST (D-FAUST) [4], focuses on human body dynamics and includes 10 subjects and 129 sequences with a split of training (70%), validation (10%), and testing (20%) subsets. The second, DeformingThings4D-Animals (DT4D-A) [29], includes 38 identities with a total of 1227 animations, divided into training (75%), validation (7.5%), and test (17.5%) subsets. The training and validation sets are sequences of seen individuals and motions. The test sets are divided into unseen motions and unseen individuals.

Baselines: Our model’s performance in 4D reconstruction is benchmarked against leading methods: OFlow [36], LPDC [52], and CaDex [26]. **OFlow** employs a Neural-ODE framework [9] to learn shape transformations, representing a distinct approach in 4D modeling. **LPDC**, in contrast, utilizes an MLP-based method for deformation processing, offering a different perspective from OFlow. **CaDex** introduces a unique approach by employing a learned canonical shape for improved stability, setting a novel standard for comparison. To ensure fair evaluation, all methods were tested following the training paradigm established by OFlow [36] for D-FAUST [4], and CaDex [26] for DT4D-A [29], providing a consistent basis for comparison.

Input	Method	Unseen Motion			Unseen Individual		
		IoU \uparrow	CD \downarrow	Corr \downarrow	IoU \uparrow	CD \downarrow	Corr \downarrow
DT4D-A	OFlow [36]	70.6%	0.104	0.204	57.3%	0.175	0.285
	LPDC [52]	72.4%	0.085	0.162	59.4%	0.149	0.262
	CaDex [26]	80.3%	0.061	0.133	64.7%	0.127	0.239
	Ours	88.9%	0.050	0.061	83.7%	0.058	0.074
D-FAUST	OFlow [36]	81.5%	0.065	0.094	72.3%	0.084	0.117
	LPDC [52]	84.9%	0.055	0.080	76.2%	0.071	0.098
	CaDex [26]	89.1%	0.039	0.070	80.7%	0.055	0.087
	Ours	90.7%	0.032	0.041	84.1%	0.044	0.054

Table 1. Quantitative comparisons of 4D Shape Reconstruction from **sparse and noisy** point cloud sequences on the DT4D-A [29] and the D-FAUST [4] datasets.

son across the different methodologies.

Evaluation Metrics: We follow [36, 52] and use same metrics. The Intersection over Union (IoU) metric evaluates the overlap between predicted and ground truth meshes; higher IoU values indicate superior accuracy. The Chamfer distance, a bidirectional metric, calculates the average nearest-neighbor distance between two point sets. Lower chamfer distance values imply a closer approximation to the ground truth. We also utilized the ℓ_2 -distance error, which measures the Euclidean distance between corresponding points on the predicted and ground truth meshes, with lower values reflecting higher fidelity.

Implementations: In our two-stage training approach, the first stage involves a shape and deformation auto-encoder. The input point cloud with $N = 2048$ points is randomly sampled from the object surface and the near-surface region. We trained the auto-encoders on two NVIDIA RTX 4090 GPUs with 24 GB memory each, using a batch size of 24 for 100 epochs. The learning rate is set to 10^{-4} , with KL-divergence loss weights at 10^{-3} (shape) and 10^{-6} (deformation). We choose the number of latent codes $M = 512$ with $C = 32$ channels. The second stage is the shape and deformation diffusion, we leverage 2048 surface points and the encoder we obtained in the first stage to get the target latent codes for diffusion models. We maintained the same learning rate 10^{-4} and trained for 50 epochs.

4.1. 4D Shape Reconstruction

We initially assessed our models’ ability for 4D reconstruction from sparse and noisy point cloud sequences. Consistent with the setup in OFlow [36], our network processed sequences of $T = 17$ continuous frames. Each frame represented a sparse point cloud with a size of $L = 300$ for D-FAUST [4] or $L = 512$ for DT4D-A [29]. We also simulate noisy observations by augmenting them with Gaussian noise with a standard deviation of 0.05.

Quantitatively, our model demonstrates superior performance over state-of-the-art models on the D-FAUST [4] and DT4D-A [29] datasets, as detailed in Table 1. This superi-

Input	Method	Unseen Motion			Unseen Individual		
		IoU \uparrow	CD \downarrow	Corr \downarrow	IoU \uparrow	CD \downarrow	Corr \downarrow
DT4D-A	OFlow [36]	64.2%	0.305	0.423	55.1%	0.408	0.538
	LPDC [52]	62.2%	0.339	0.427	51.6%	0.467	0.488
	CaDex [26]	70.8%	0.254	0.499	59.2%	0.379	0.498
	Ours	73.3%	0.177	0.404	66.3%	0.193	0.438
D-FAUST	OFlow [36]	76.9%	0.084	0.165	66.4%	0.109	0.194
	LPDC [52]	68.3%	0.138	0.167	59.6%	0.156	0.204
	CaDex [26]	80.7%	0.074	0.123	70.4%	0.096	0.157
	Ours	83.8%	0.054	0.111	74.4%	0.075	0.140

Table 2. Quantitative comparisons of 4D Shape Completion from **monocular noisy depth scans** on the DT4D-A [29] and the D-FAUST [4] datasets.

ority is particularly notable in the unseen individual category of the DT4D-A dataset, which features more diverse topologies from various animals. Here, our model achieves an IoU that is 19% higher than the preceding state-of-the-art model. Additionally, both the chamfer distance and the ℓ_2 -correspondence error are reduced to less than half of those recorded by the previous state-of-the-art methods.

Qualitatively, as illustrated in Figure 6 through chamfer distance error maps, our model outperforms in reconstructing complete shapes and minimizing chamfer distance errors, particularly in capturing fast-moving structures like feet of humans and heads of animals.

The superiority of our model is attributed to the proposed 4D latent vector set diffusion, enabling more precise capture of local geometry and deformation patterns. Methods like LPDC [52] and OFlow [36] perform well in human settings thanks to similar human topologies, while CaDex [26] benefits from canonical shape learning. However, the diverse topologies and scales in animal setup, such as between species like foxes and dragons, present a significant challenge for models that optimize global codes. Our approach, in contrast, effectively captures these complex 4D dynamics of general non-rigid objects.

4.2. 4D Shape Completion

4.2.1 Monocular Depth Sequences

To simulate sparse and partial real-world scans, we generated monocular depth sequences by rendering from a fixed camera angle. The size of the point cloud input and the frame length are the same as Sec. 4.1.

The qualitative and quantitative comparisons are presented in Figure 6 and Table 2, respectively. As seen, our method consistently outperforms all state-of-the-art methods in all metrics and produces more complete surface geometries with more plausible motion tracking. This demonstrates the effectiveness of the motion priors learned by our proposed 4D latent set diffusion in addressing ambiguous data like partial observations.

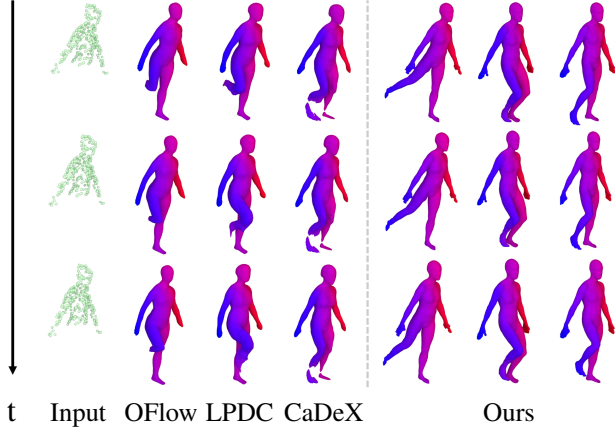


Figure 7. Comparisons of 4D Shape Reconstruction from **highly partial** point cloud sequences, such as half-body scans obtained from the D-FAUST [4] dataset. The colors of the meshes encode the correspondence. Our diffusion-based method produces highly complete human shapes with more favorable motions, providing multiple possible outputs that match the input observations.

4.2.2 Partial Scan Sequences

To assess the robustness of our method to extremely ambiguous data, we set up a challenging experiment on the D-FAUST [4] dataset. This involved reconstructing whole body motions based on partial point clouds of the upper bodies. This setup creates a highly ambiguous scenario, as the same upper body motion can correspond to many different lower-body. We adopt the same configuration as Sec. 4.1, with a frame length ($T = 17$) and input point cloud size ($L = 300$). OFlow [36], LPDC [52], and CaDeX [26] encounter challenges in reconstructing the complete shape, often producing distorted shapes such as broken feet. In contrast, our method excels in reconstructing more complete geometries while achieving temporally coherent tracking. Additionally, our approach presents a diverse range of plausible full-body reconstructions that align with the given upper-body scans. The superior performance of our model is primarily attributed to the 4D latent vector set diffusion. Our diffusion-based method is more capable of tackling the ‘one-to-many’ complexities from extremely partial data.

4.3. Ablation Study

We conducted detailed ablation studies to validate the effectiveness of each design (See Table 3).

What is the effect of latent vector set representation?

Instead of using global latent codes to represent shapes and time-varying deformations, our approach employs 4D latent vector sets. As indicated by Table 3 (with $M = 1$), our method significantly outperforms the variant using global

Method	Unseen Motion			Unseen Individual		
	IoU \uparrow	CD \downarrow	Corr \downarrow	IoU \uparrow	CD \downarrow	Corr \downarrow
$M = 1$	68.5%	0.120	0.301	57.7%	0.149	0.327
$C = 8$	78.9%	0.078	0.180	68.0%	0.105	0.225
$C = 16$	78.0%	0.080	0.189	66.8%	0.109	0.254
w/o. TimeAttn.	81.2%	0.061	0.127	70.8%	0.086	0.158
Full	83.8%	0.054	0.111	74.4%	0.075	0.140

Table 3. Quantitative ablation studies on the D-FAUST [4] dataset. M denotes the number of latent codes and C represents the number of latent code channels.

latent codes, achieving a 15.3 % improvement in IoU for unseen motion reconstruction. This highlights the superior ability of 4D latent sets to accurately capture 4D motions. The advantage becomes even more apparent with a 16.7 % improvement in unseen identities, demonstrating enhanced generalization ability to objects with different structures.

What is the effect of time attention layers? For the synchronized deformation latent set diffusion, we have integrated the time self-attention layer in our interleaved spatio-temporal attention mechanism. We attempted to remove the layer. However, the results exhibited a decrease in all metrics, emphasizing the effectiveness of the time self-attention layer in maintaining temporal coherence.

What is the effect of the number of channels of latent set?

To determine the optimal configuration for learning shape and deformation priors within time-varying deformable surfaces, we varied the channel numbers (8, 16, 32) of the shape and deformation latent sets. Experimental results indicated that using 32 channels for 4D latent set diffusion is more suitable, obtaining more favorable results.

5. Conclusion

We present Motion2VecSets, a 4D diffusion model for dynamic surface reconstruction from point cloud sequences. Our method explicitly models the shape and motion distribution of non-rigid objects through an iterative denoising process of compressed latent vector sets, generating plausible and diverse outputs. The learned shape and motion diffusion priors can effectively deal with ambiguous observations, including sparse, noisy, and partial data. Compared to encoding shape and deformation with a global latent, our novel 4D latent vector set representation enables more accurate non-linear motion capture and improves the generalizability to unseen identities and motions. The designed interleaved space and time attention block for synchronized deformation vector sets diffusion enforces temporal-coherent object tracking while reducing computational overhead. Extensive experiments on reconstructing sparse, partial, and even half bodies on the D-FAUST [4] and the DT4D-A [29]

demonstrate the superiority of our approaches for various imperfect observations. We believe our Motion2VecSets can be future extended with multi-modalities such as text or speech-driven 4D generation.

Acknowledgement. This work was supported by the ERC Starting Grant Scan2CAD (804724) as well as the German Research Foundation (DFG) Research Unit “Learning and Simulation in Visual Computing”. We further thank Angela Dai for the video voice-over.

References

- [1] Panos Achlioptas, Olga Diamanti, Ioannis Mitliagkas, and Leonidas J Guibas. Learning representations and generative models for 3d point clouds. *arXiv preprint arXiv:1707.02392*, 2017. 2
- [2] Bharat Lal Bhatnagar, Xianghui Xie, Ilya Petrov, Cristian Sminchisescu, Christian Theobalt, and Gerard Pons-Moll. Behave: Dataset and method for tracking human object interactions. In *IEEE Conference on Computer Vision and Pattern Recognition (CVPR)*. IEEE, 2022. 18
- [3] Andreas Blattmann, Robin Rombach, Kaan Oktay, and Björn Ommer. Retrieval-augmented diffusion models, 2022. 3
- [4] Federica Bogo, Javier Romero, Gerard Pons-Moll, and Michael J. Black. Dynamic FAUST: Registering human bodies in motion. In *IEEE Conf. on Computer Vision and Pattern Recognition (CVPR)*, 2017. 2, 6, 7, 8, 14, 15, 16, 18, 19, 21
- [5] Aljaž Božič, Pablo Palafox, Michael Zollhöfer, Justus Thies, Angela Dai, and Matthias Nießner. Neural deformation graphs for globally-consistent non-rigid reconstruction. *CVPR*, 2021. 2
- [6] Rohan Chabra, Jan Eric Lenssen, Eddy Ilg, Tanner Schmidt, Julian Straub, Steven Lovegrove, and Richard Newcombe. Deep local shapes: Learning local sdf priors for detailed 3d reconstruction, 2020. 2
- [7] Chao Chen, Yu-Shen Liu, and Zhizhong Han. Gridpull: Towards scalability in learning implicit representations from 3d point clouds. In *Proceedings of the IEEE International Conference on Computer Vision (ICCV)*, 2023. 2
- [8] Nanxin Chen, Yu Zhang, Heiga Zen, Ron J. Weiss, Mohammad Norouzi, and William Chan. Wavegrad: Estimating gradients for waveform generation, 2020. 3
- [9] Ricky TQ Chen, Yulia Rubanova, Jesse Bettencourt, and David K Duvenaud. Neural ordinary differential equations. *Advances in neural information processing systems*, 31, 2018. 6
- [10] Zhiqin Chen and Hao Zhang. Learning implicit fields for generative shape modeling. *Proceedings of IEEE Conference on Computer Vision and Pattern Recognition (CVPR)*, 2019. 2
- [11] Julian Chibane, Thiemo Alldieck, and Gerard Pons-Moll. Implicit functions in feature space for 3d shape reconstruction and completion. In *IEEE Conference on Computer Vision and Pattern Recognition (CVPR)*. IEEE, 2020. 2
- [12] Gene Chou, Yuval Bahat, and Felix Heide. Diffusion-sdf: Conditional generative modeling of signed distance functions. 2023. 3
- [13] Christopher B Choy, Danfei Xu, JunYoung Gwak, Kevin Chen, and Silvio Savarese. 3d-r2n2: A unified approach for single and multi-view 3d object reconstruction. In *Proceedings of the European Conference on Computer Vision (ECCV)*, 2016. 2
- [14] Rishabh Dabral, Muhammad Hamza Mughal, Vladislav Golyanik, and Christian Theobalt. Mofusion: A framework for denoising-diffusion-based motion synthesis. In *Proceedings of the IEEE/CVF Conference on Computer Vision and Pattern Recognition*, pages 9760–9770, 2023. 3
- [15] Prafulla Dhariwal and Alex Nichol. Diffusion models beat gans on image synthesis, 2021. 3
- [16] Haoqiang Fan, Hao Su, and Leonidas J Guibas. A point set generation network for 3d object reconstruction from a single image. In *Proceedings of the IEEE conference on computer vision and pattern recognition*, pages 605–613, 2017. 2
- [17] Matheus Gadelha, Subhransu Maji, and Rui Wang. 3d shape induction from 2d views of multiple objects. In *2017 International Conference on 3D Vision (3DV)*, pages 402–411, 2017. 2
- [18] Amos Gropp, Lior Yariv, Niv Haim, Matan Atzmon, and Yaron Lipman. Implicit geometric regularization for learning shapes. In *Proceedings of Machine Learning and Systems 2020*, pages 3569–3579. 2020. 2
- [19] Thibault Groueix, Matthew Fisher, Vladimir G. Kim, Bryan Russell, and Mathieu Aubry. AtlasNet: A Papier-Mâché Approach to Learning 3D Surface Generation. In *Proceedings IEEE Conf. on Computer Vision and Pattern Recognition (CVPR)*, 2018. 2
- [20] X. Han, Z. Li, H. Huang, E. Kalogerakis, and Y. Yu. High-resolution shape completion using deep neural networks for global structure and local geometry inference. In *IEEE International Conference on Computer Vision (ICCV)*, pages 85–93, Los Alamitos, CA, USA, 2017. IEEE Computer Society. 2
- [21] Jonathan Ho, Ajay Jain, and Pieter Abbeel. Denoising diffusion probabilistic models, 2020. 2
- [22] Jonathan Ho, Tim Salimans, Alexey Gritsenko, William Chan, Mohammad Norouzi, and David J Fleet. Video diffusion models. *arXiv:2204.03458*, 2022. 3
- [23] Karl Holmquist and Bastian Wandt. Diffpose: Multi-hypothesis human pose estimation using diffusion models. In *Proceedings of the IEEE/CVF International Conference on Computer Vision*, pages 15977–15987, 2023. 3
- [24] Boyan Jiang, Yinda Zhang, Xingkui Wei, Xiangyang Xue, and Yanwei Fu. Learning compositional representation for 4d captures with neural ode. In *CVPR*, 2021. 2
- [25] Tero Karras, Miika Aittala, Timo Aila, and Samuli Laine. Elucidating the design space of diffusion-based generative models. In *Proc. NeurIPS*, 2022. 4
- [26] Jiahui Lei and Kostas Daniilidis. Cadex: Learning canonical deformation coordinate space for dynamic surface representation via neural homeomorphism. In *Proceedings of the IEEE/CVF Conference on Computer Vision and Pattern Recognition*, 2022. 1, 2, 3, 4, 6, 7, 8, 12, 14, 15

- [27] Jiahui Lei, Congyue Deng, Bokui Shen, Leonidas Guibas, and Kostas Daniilidis. Nap: Neural 3d articulation prior, 2023. [2](#), [3](#)
- [28] Tianye Li, Timo Bolkart, Michael J. Black, Hao Li, and Javier Romero. Learning a model of facial shape and expression from 4D scans. *ACM Transactions on Graphics, (Proc. SIGGRAPH Asia)*, 36(6):194:1–194:17, 2017. [1](#), [2](#), [4](#)
- [29] Yang Li, Hikari Takehara, Takafumi Taketomi, Bo Zheng, and Matthias Nießner. 4dcomplete: Non-rigid motion estimation beyond the observable surface. *IEEE International Conference on Computer Vision (ICCV)*, 2021. [1](#), [2](#), [6](#), [7](#), [8](#), [14](#), [15](#), [17](#), [18](#), [20](#), [22](#)
- [30] Yiyi Liao, Simon Donné, and Andreas Geiger. Deep marching cubes: Learning explicit surface representations. In *Conference on Computer Vision and Pattern Recognition (CVPR)*, 2018. [2](#)
- [31] Matthew Loper, Naureen Mahmood, Javier Romero, Gerard Pons-Moll, and Michael J. Black. SMPL: A skinned multi-person linear model. *ACM Trans. Graphics (Proc. SIGGRAPH Asia)*, 34(6):248:1–248:16, 2015. [1](#), [2](#), [15](#)
- [32] Shitong Luo and Wei Hu. Diffusion probabilistic models for 3d point cloud generation. In *Proceedings of the IEEE/CVF Conference on Computer Vision and Pattern Recognition (CVPR)*, 2021. [3](#)
- [33] Lars Mescheder, Michael Oechsle, Michael Niemeyer, Sebastian Nowozin, and Andreas Geiger. Occupancy networks: Learning 3d reconstruction in function space. In *Proceedings IEEE Conf. on Computer Vision and Pattern Recognition (CVPR)*, 2019. [2](#), [15](#)
- [34] Gautam Mittal, Jesse Engel, Curtis Hawthorne, and Ian Simon. Symbolic music generation with diffusion models, 2021. [3](#)
- [35] Alex Nichol, Prafulla Dhariwal, Aditya Ramesh, Pranav Shyam, Pamela Mishkin, Bob McGrew, Ilya Sutskever, and Mark Chen. Glide: Towards photorealistic image generation and editing with text-guided diffusion models, 2022. [3](#)
- [36] Michael Niemeyer, Lars Mescheder, Michael Oechsle, and Andreas Geiger. Occupancy flow: 4d reconstruction by learning particle dynamics. In *International Conference on Computer Vision*, 2019. [2](#), [3](#), [4](#), [6](#), [7](#), [8](#), [12](#), [15](#)
- [37] Ahmed A A Osman, Timo Bolkart, and Michael J. Black. STAR: A sparse trained articulated human body regressor. In *European Conference on Computer Vision (ECCV)*, pages 598–613, 2020. [1](#), [2](#), [4](#)
- [38] Pablo Palafox, Aljaž Božič, Justus Thies, Matthias Nießner, and Angela Dai. Npms: Neural parametric models for 3d deformable shapes. *arXiv preprint arXiv:2104.00702*, 2021. [2](#)
- [39] Junyi Pan, Xiaoguang Han, Weikai Chen, Jiapeng Tang, and Kui Jia. Deep mesh reconstruction from single rgb images via topology modification networks. In *Proceedings of the IEEE International Conference on Computer Vision*, pages 9964–9973, 2019. [2](#)
- [40] Jeong Joon Park, Peter Florence, Julian Straub, Richard Newcombe, and Steven Lovegrove. DeepSDF: Learning continuous signed distance functions for shape representation. In *The IEEE Conference on Computer Vision and Pattern Recognition (CVPR)*, 2019. [2](#)
- [41] Songyou Peng, Michael Niemeyer, Lars Mescheder, Marc Pollefeys, and Andreas Geiger. Convolutional occupancy networks. In *European Conference on Computer Vision (ECCV)*, 2020. [3](#)
- [42] Charles R Qi, Hao Su, Kaichun Mo, and Leonidas J Guibas. Pointnet: Deep learning on point sets for 3d classification and segmentation. *arXiv preprint arXiv:1612.00593*, 2016. [3](#)
- [43] Zhiyuan Ren, Zhihong Pan, Xin Zhou, and Le Kang. Diffusion motion: Generate text-guided 3d human motion by diffusion model, 2023. [3](#)
- [44] Gernot Riegler, Ali Osman Ulusoy, and Andreas Geiger. Octnet: Learning deep 3d representations at high resolutions. In *Proceedings of the IEEE Conference on Computer Vision and Pattern Recognition*, 2017. [2](#)
- [45] Robin Rombach, Andreas Blattmann, Dominik Lorenz, Patrick Esser, and Björn Ommer. High-resolution image synthesis with latent diffusion models, 2021. [3](#), [4](#), [12](#)
- [46] Javier Romero, Dimitrios Tzionas, and Michael J. Black. Embodied hands: Modeling and capturing hands and bodies together. *ACM Transactions on Graphics, (Proc. SIGGRAPH Asia)*, 36(6), 2017. [1](#), [2](#), [4](#)
- [47] Mingyi Shi, Sebastian Starke, Yuting Ye, Taku Komura, and Jungdam Won. Phasemp: Robust 3d pose estimation via phase-conditioned human motion prior. In *Proceedings of the IEEE/CVF International Conference on Computer Vision (ICCV)*, pages 14725–14737, 2023. [3](#)
- [48] David Stutz and Andreas Geiger. Learning 3d shape completion from laser scan data with weak supervision. In *IEEE Conference on Computer Vision and Pattern Recognition (CVPR)*. IEEE Computer Society, 2018. [2](#)
- [49] Jiapeng Tang, Xiaoguang Han, Junyi Pan, Kui Jia, and Xin Tong. A skeleton-bridged deep learning approach for generating meshes of complex topologies from single rgb images. In *The IEEE Conference on Computer Vision and Pattern Recognition (CVPR)*, 2019. [2](#)
- [50] Jiapeng Tang, Xiaoguang Han, Minghui Tan, Xin Tong, and Kui Jia. Skeletonnet: A topology-preserving solution for learning mesh reconstruction of object surfaces from rgb images, 2021. [2](#)
- [51] Jiapeng Tang, Jiabao Lei, Dan Xu, Feiying Ma, Kui Jia, and Lei Zhang. Sa-convnet: Sign-agnostic optimization of convolutional occupancy networks, 2021. [2](#)
- [52] Jiapeng Tang, Dan Xu, Kui Jia, and Lei Zhang. Learning parallel dense correspondence from spatio-temporal descriptors for efficient and robust 4d reconstruction. In *Proceedings of the IEEE/CVF Conference on Computer Vision and Pattern Recognition*, pages 6022–6031, 2021. [2](#), [3](#), [4](#), [6](#), [7](#), [8](#), [12](#), [15](#)
- [53] Jiapeng Tang, Angela Dai, Yinyu Nie, Lev Markhasin, Justus Thies, and Matthias Niessner. Dphms: Diffusion parametric head models for depth-based tracking, 2023. [3](#)
- [54] Jiapeng Tang, Lev Markhasin, Bi Wang, Justus Thies, and Matthias Nießner. Neural shape deformation priors, 2023. [2](#), [14](#)
- [55] Jiapeng Tang, Yinyu Nie, Lev Markhasin, Angela Dai, Justus Thies, and Matthias Nießner. Diffuscene: Scene graph denoising diffusion probabilistic model for generative indoor scene synthesis, 2023. [3](#)

- [56] Gerald Teschl. *Ordinary differential equations and dynamical systems*. American Mathematical Soc., 2012. 2
- [57] Guy Tevet, Sigal Raab, Brian Gordon, Yonatan Shafir, Daniel Cohen-Or, and Amit H Bermano. Human motion diffusion model. *arXiv preprint arXiv:2209.14916*, 2022. 3
- [58] Edgar Tretschk, Ayush Tewari, Vladislav Golyanik, Michael Zollhöfer, Carsten Stoll, and Christian Theobalt. Patch-Nets: Patch-Based Generalizable Deep Implicit 3D Shape Representations. *European Conference on Computer Vision (ECCV)*, 2020. 2
- [59] Nanyang Wang, Yinda Zhang, Zhuwen Li, Yanwei Fu, Wei Liu, and Yu-Gang Jiang. Pixel2mesh: Generating 3d mesh models from single rgb images. In *ECCV*, 2018. 2
- [60] Ye Yuan, Jiaming Song, Umar Iqbal, Arash Vahdat, and Jan Kautz. Physdiff: Physics-guided human motion diffusion model. In *Proceedings of the IEEE/CVF International Conference on Computer Vision*, pages 16010–16021, 2023. 3
- [61] Biao Zhang, Jiapeng Tang, Matthias Nießner, and Peter Wonka. 3dshape2vecset: A 3d shape representation for neural fields and generative diffusion models. *ACM Trans. Graph.*, 42(4), 2023. 2, 4
- [62] Mingyuan Zhang, Zhongang Cai, Liang Pan, Fangzhou Hong, Xinying Guo, Lei Yang, and Ziwei Liu. Motiondiffuse: Text-driven human motion generation with diffusion model, 2022. 3
- [63] Hengshuang Zhao, Li Jiang, Jiaya Jia, Philip HS Torr, and Vladlen Koltun. Point transformer. In *Proceedings of the IEEE/CVF International Conference on Computer Vision*, pages 16259–16268, 2021. 2
- [64] Denis Zorin, Peter Schröder, and Wim Sweldens. Interpolating subdivision for meshes with arbitrary topology. In *Proceedings of the 23rd annual conference on Computer graphics and interactive techniques*, pages 189–192, 1996. 15
- [65] Silvia Zuffi, Angjoo Kanazawa, David Jacobs, and Michael J. Black. 3D menagerie: Modeling the 3D shape and pose of animals. In *IEEE Conf. on Computer Vision and Pattern Recognition (CVPR)*, 2017. 1, 2, 4

Appendix

In this supplementary material, we complement our main paper with additional details. It begins with an introduction to the notations used in our paper in Sec. A. The following section, Sec. B, discusses our network architectures, highlighting key design choices and their impact. This is complemented by Sec. C, which provides essential implementation details. We then show more comparisons between our approach with established methods like OFlow [36], LPDC [52], and CaDeX [26] in Sec. D, offering insights into our model’s strengths and improvements. Finally, in Sec. E, we demonstrate the real-world applicability of our model, underscoring its practical effectiveness.

A. Notations

In this paper, we use the following notations, as summarized in Tab. 4. The symbol T represents the sequence length, with the superscript t indicating the time step of a frame in the sequence. Our network’s input is a sparse or partial point cloud, denoted as $\mathcal{P} = \{\mathbf{P}^t\}_{t=0}^{T-1}$, where each frame \mathbf{P}^t comprises L points, serving as conditions in reference time. The sets $\mathcal{S}, \mathcal{D}, \mathcal{C}$ represent shape codes, deformation codes, and conditional codes, respectively, with each i -th code denoted by the corresponding lowercase letter. The mesh is symbolized by $\mathcal{M} = \{\mathcal{V}, \mathcal{F}\}$, where \mathcal{V} and \mathcal{F} correspond to the vertices and faces set of the mesh. Furthermore, \mathbf{X} refers to surface points sampled from ground truth meshes for learning shape, we dedicate $\mathbf{X}_{\text{src}}, \mathbf{X}_{\text{tgt}}$ for representing the sampled surface points for learning deformation. Moreover, \mathcal{Q} represents the set of query points, where \mathbf{q} refers to a point inside the point set and \mathbf{q}' is the output by feeding the query point into the deformation network.

B. Network Architectures

The inputs of our model are a sequence of T frames of sparse or partial noisy point clouds, represented by $\mathcal{P} = \{\mathbf{P}^t\}_{t=1}^T$, where $\mathbf{P}^t = \{\mathbf{p}_i \in \mathbb{R}^3\}_{i=1}^L$, L represents the number of points. The goal is to reconstruct continuous 3D meshes with high fidelity, denoted as $\{\mathcal{M}^t\}_{t=1}^T = \{\mathcal{V}^t, \mathcal{F}^t\}_{t=1}^T$, where \mathcal{V}^t and \mathcal{F}^t refer to the set of vertices faces of the reconstructed mesh at time frame t .

B.1. Shape Diffusion

In the shape diffusion part, we leverage the first frame of the sequence, \mathbf{P}^1 , to reconstruct the object shape. As illustrated in Fig. 8, this process is divided into two distinct networks: (a) *Shape Autoencoder Network* and (b) *Shape Vector Set Diffusion Network*.

Shape Autoencoder In the *Shape Autoencoder Network*, points \mathbf{X}^1 , surface and near-surface points sampled from

Symbol	Meaning
T	# frames
$\mathcal{P} = \{\mathbf{P}^t\}_{t=0}^{T-1}$	Sparse point clouds as input for diffusion models
$\mathbf{P}^t = \{\mathbf{p}_i \in \mathbb{R}^3\}_{i=0}^L$	A frame of sparse point clouds
L	# points in sparse point clouds
$\mathcal{S} = \{\mathbf{s}_i \in \mathbb{R}^C\}_{i=0}^M$	One set of shape codes with M latent codes
s_i	i -th shape code
$\mathcal{D} = \{\mathbf{d}_i \in \mathbb{R}^C\}_{i=0}^M$	One set of deformation codes with M latent codes
d_i	i -th deformation code
$\mathcal{C} = \{\mathbf{c}_i \in \mathbb{R}^C\}_{i=0}^M$	One set of conditional codes with M latent codes
c_i	i -th deformation code
C	# latent code channels
\mathcal{V}, \mathcal{F}	Vertices and faces of mesh
\mathbf{X}	Points sample from meshes as input for shape autoencoder
$\mathbf{X}_{\text{src}}, \mathbf{X}_{\text{tgt}}$	Points sample from source and target meshes as input for deformation autoencoder
\mathcal{Q}	Query points set
\mathbf{q}	Query point
\mathbf{q}'	Deformed query point

Table 4. **Notation table** includes the mathematical symbols we mentioned in the paper.

the first frame’s mesh. To optimize computational efficiency, we adopt the furthest point sampling (FPS) technique. This method pinpoints crucial points within a point cloud, thereby thinning its density:

$$\mathbf{X} = \text{FPS}(\mathbf{X}_0) \quad (8)$$

Subsequently, a cross-attention block, designed to compute attention weights across various points, is employed. This block fuses the features of the subsampled points and generates a shape latent set, denoted as $\mathcal{S} = \{\mathbf{s}_i \in \mathbb{R}^C\}_{i=1}^M$. Here, M represents the overall count of codes and C denotes their dimensionality. In this process, the positional embeddings derived from the points after FPS sampling are utilized as the query, whereas those obtained before FPS sampling serve as the key and value in the attention mechanism. Also, consistent with the latent diffusion framework proposed by [45], our model incorporates KL-regularization within the

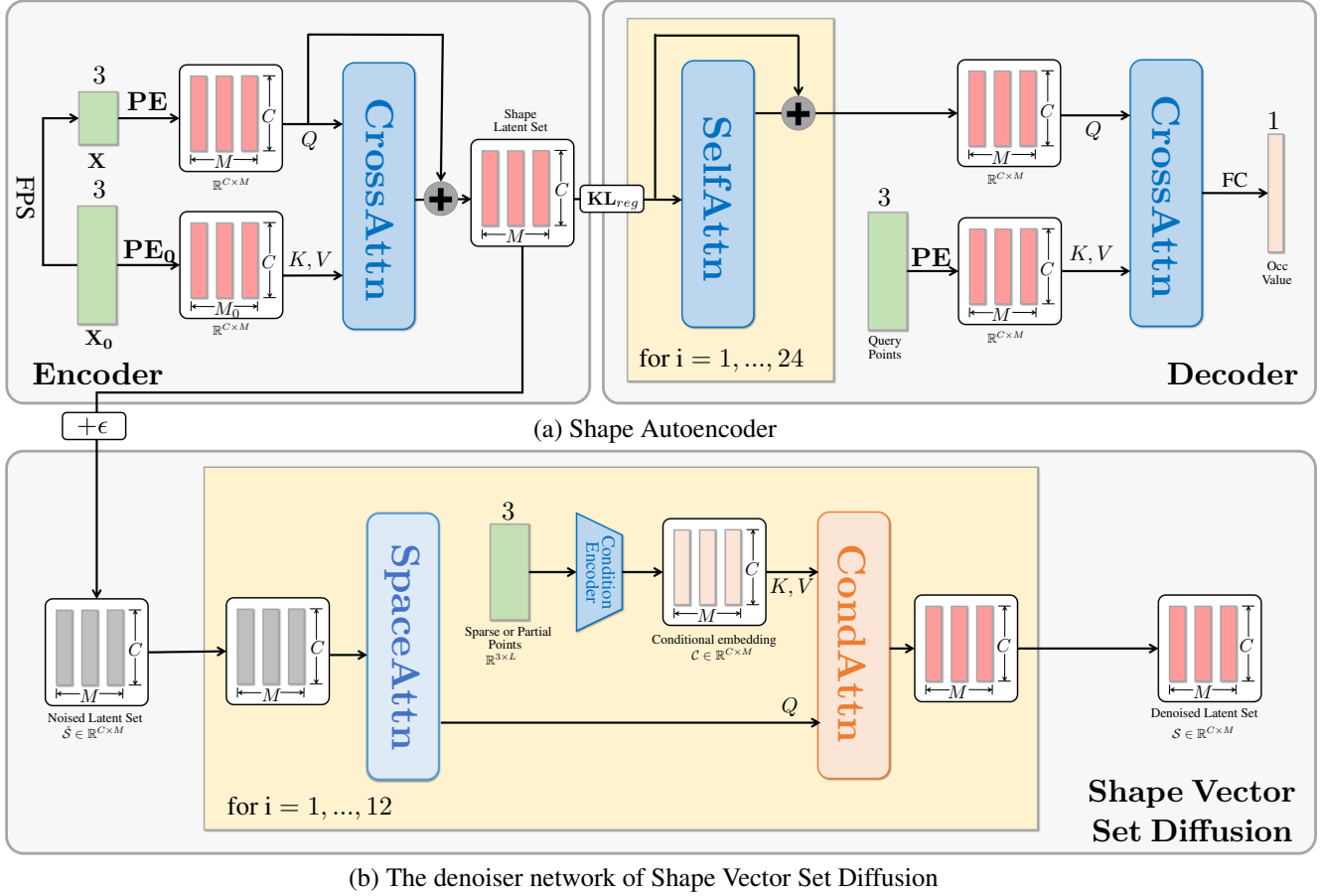


Figure 8. Network architecture of **Shape Diffusion**

latent space. This regularization strategy plays a crucial role in modulating feature diversity, ensuring the preservation of high-level features. The query points are encoded and passed to the cross-attention block with the generated shape code. The resulting fused code is then mapped to a dimension of 1 via a fully connected (FC) layer, providing the predicted occupancy value for the query points.

Shape Vector Set Diffusion Noised shape codes \hat{S} are sent to the denoising neural network. The denoiser consists of two blocks: The space-attention block facilitates positional information exchange among M codes in different positions, while the condition-attention block injects information from sparse or partial points (conditional input). After repeating this process, a denoised latent set, S is obtained.

B.2. Synchronized Deformation Diffusion

As shown in Fig. 9, the deformation encoding part is also split into two parts: *Deformation Autoencoder Network* and *Synchronized Deformation Vector Set Diffusion Network*.

Deformation Autoencoder In the deformation autoencoder, both surface and near-surface points of different frames are sampled according to the same face indexes, which ensures the correspondence within a sequence. These point cloud frames are pairwise paired together, each with a source point cloud $\mathbf{X}_{\text{src}0}$ and a target point cloud $\mathbf{X}_{\text{tgt}0}$.

Similarly to shape diffusion, to ensure the correspondence between the source point cloud and the target point cloud, we use the same FPS for downsampling. We have:

$$\mathbf{X}_{\text{scr}} = \text{FPS}(\mathbf{X}_{\text{scr}0}) \quad (9)$$

$$\mathbf{X}_{\text{tgt}} = \text{FPS}(\mathbf{X}_{\text{tgt}0}) \quad (10)$$

As shown in Fig. 9 (a), after obtaining the key points of the source and target point clouds. Positional embeddings of the FPS downsampled and original point clouds are concatenated along the last dimension to preserve spatial consistency, where $\text{PosEmb}: \mathbb{R}^3 \rightarrow \mathbb{R}^M$ refers to positional embedding functions:

$$\mathbf{PE} = \text{Concat}(\text{PosEmb}(\mathbf{X}_{\text{src}}), \text{PosEmb}(\mathbf{X}_{\text{tgt}})) \quad (11)$$

$$\mathbf{PE}_0 = \text{Concat}(\text{PosEmb}(\mathbf{X}_{\text{src}0}), \text{PosEmb}(\mathbf{X}_{\text{tgt}0})) \quad (12)$$

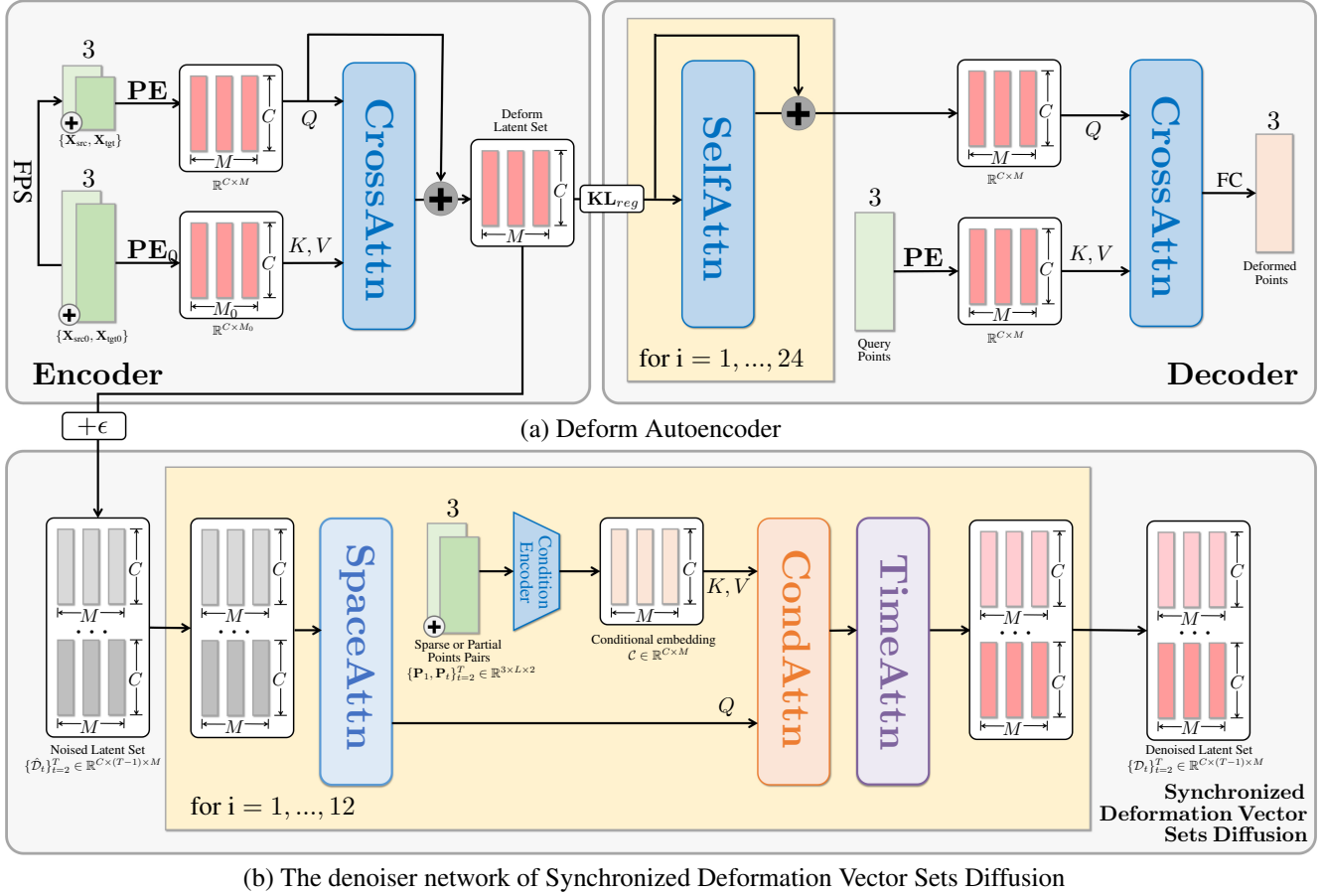


Figure 9. Network architecture of **Synchronized Deformation Diffusion**.

We employ the cross attention operation $\text{CrossAttn}(Q, KV)$ throughout our method, where Q denotes the query, and KV denotes the key-value pair. Similarly, we use KL-divergence to retain high-level features to facilitate the learning of the diffusion model. Here we get the deformation latent set $\mathcal{D} = \{\mathbf{d}_i \in \mathbb{R}^C\}_{i=1}^M$:

$$\mathcal{D}(\mathbf{X}_{\text{src}}, \mathbf{X}_{\text{tgt}}) = \text{CrossAttn}(\text{PE}, \text{PE}_0) \quad (13)$$

In inference time, we take the surface points of the source mesh as query points. The interaction between the predicted deformation codes sampled from the *Shape Vector Set Diffusion Network* and the positional embedding of query points through cross-attention yields the approximated latent features. Subsequently, a linear layer derives the predicted positions of the target point cloud.

Synchronized Deformation Vector Set Diffusion In this stage, the sparse noisy input point clouds $\{\mathbf{P}_{\text{src}}, \mathbf{P}_{\text{tgt}}\}$ pairs green blocks in Fig. 9 (b) are processed with a conditional encoder. The conditional encoder has the same structure with the deformation encoder, through which we get the conditional latent set $\mathcal{C}^t(\mathbf{P}^1, \mathbf{P}^t) = \{\mathbf{c}_i \in \mathbb{R}^C\}_{i=1}^M$. In

the meanwhile, the shape latent set from the deformation encoder is added with Gaussian noise and sent to the denoiser of the diffusion model. As illustrated in the figure, after the space self-attention block, the conditional latent set is injected into the cross-attention block, after the cross-attention along the temporal domain, we get the denoised deformation codes. This process is repeated for 18 times by default.

C. Implementation Details

C.1. Dataset

Train/Val/Test Split The datasets used in our method, D-FAUST [4] and DT4D-A [29], encompass a diverse range of human and animal motions, respectively. D-FAUST includes human motions like “chicken wings”, “shake shoulders”, and “shake hips.” In contrast, DT4D-A features animal animations such as “bear3EP death”, “bunnyQ walk”, and “deer2MB rotate.” Following the approach in NSDP [54] and CaDeX [26], we organize our train and validation sets with data from seen identities performing seen motions. The test set is divided into two categories: unseen motions

of seen identities and seen motions of unseen identities. Specifically, for DT4D-A [29], our training set comprises 835 sequences, the validation set includes 59 sequences, and the test set is divided into 89 sequences for unseen motions and 108 sequences for unseen identities. Similarly, in D-FAUST [4], the training set contains 104 sequences, the validation set has 5 sequences, and the test set includes 9 sequences for unseen motions and 11 sequences for unseen identities.

Data Processing Our data processing strategy is designed to facilitate the learning of shape encoding and deformation. We utilize two distinct datasets for this purpose.

For shape encoding, our process begins with the application of the Butterfly Subdivision method [64], an interpolating subdivision technique widely used in computer graphics for generating smooth surfaces from polygonal meshes. Following the methodology outlined in [33], we center and rescale all meshes to ensure that the bounding box of each mesh is centered at the origin $(0, 0, 0)$ and the longest edge is normalized to a length of 1. We then uniformly sample 200k points within this normalized cube and compute their occupancy values to determine whether they lie inside or outside the mesh, as detailed in [33]. To enhance our model’s understanding of surface properties, we introduce Gaussian noise at two different levels to the mesh surface points. This process generates 200k near-surface points, whose occupancy values are also computed. These points, combined with an additional 200k points sampled directly from the mesh surface, constitute the input to our network, providing a comprehensive set of data points for both uniform space and near-surface regions.

For deformation encoding, we depart from using the Butterfly Subdivision method [64], which was applied in the context of shape encoding. This choice is primarily driven by the need to maintain spatial correspondence between points. To achieve this, we directly sample 200k surface points from the mesh. Subsequently, we sample an equal number of near-surface points. These near-surface points are generated along the normal direction of each surface point, with a predefined distance that ensures closeness to the surface while preserving the detail of the mesh structure. Crucially, both sets of points are selected based on the same face indices of the mesh. This methodical selection guarantees that the spatial correspondence is not disrupted, allowing for a more accurate representation of deformation.

Within the context of the partial challenge configuration, a camera was positioned with a fixed viewing angle of 45 degrees directed towards the human or animal subject within the scene. This positioning was undertaken to capture a partial depth observation of the subject, as illustrated in Figure 10. Additionally, in the more restricted partial setting, only half of the human body was observed. This

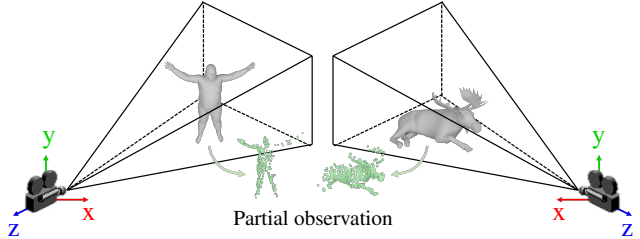


Figure 10. The camera setup for the generation of partial observation in D-FAUST [4] and DT4D-A [29] dataset.

was accomplished by intentionally selecting vertex indices corresponding to the upper body of the SMPL model [31].

D. Additional Results

D.1. 4D Shape Reconstruction

In evaluating our model’s performance in 4D shape reconstruction, we adopted a comprehensive set of metrics: Intersection over Union (IoU), chamfer distance, and correspondence distance. These metrics were chosen for their relevance in accurately quantifying shape reconstruction quality. IoU measures the overlap between predicted and ground truth shapes, Chamfer distance quantifies the average closest point distance, and correspondence distance evaluates the accuracy of point-wise correspondences. These metrics align with the standards set in recent studies, such as those by LPDC [52] and OFlow [36].

We present the average metrics across all 17 frames for both D-FAUST [4] and DT4D-A [29] datasets. The quantitative results are shown in Tab. 6, Tab. 5, Tab. 8, and Tab. 7. Our analysis reveals that our model demonstrates superior generalization capabilities in scenarios involving both unseen motions and unseen individuals. Specifically, it outperforms existing approaches, including OFlow [36], LPDC [52], and CaDeX [26], across all evaluated metrics for all time frames. This advancement underscores the efficacy of our approach in handling the complexities of 4D shape reconstruction. Furthermore, qualitative results in Fig. 12 and Fig. 13 show a selection of 8 frames, chosen to represent a diverse range of motions and shapes, from the total 17 to illustrate our model’s performance. In each figure, the upper part displays the results for unseen motion, while the lower part corresponds to unseen individuals. We utilize a chamfer distance error map for visualization, where blue indicates lower error and red signifies higher error. The color-coded error map, computed based on the distance between predicted and ground truth points, provides an intuitive understanding of the model’s accuracy in different scenarios. Our model not only has an overall smaller error on both datasets, but also captures motions more accurately.

Time step	IoU				Chamfer				Correspond.			
	OFlow	LPDC	CaDex	Ours	OFlow	LPDC	CaDex	Ours	OFlow	LPDC	CaDex	Ours
0	83.1%	85.6%	89.1%	91.2%	0.059	0.052	0.044	0.031	0.057	0.047	0.043	0.031
1	83.1%	85.5%	89.2%	91.1%	0.059	0.053	0.044	0.031	0.062	0.053	0.047	0.034
2	82.8%	85.4%	89.3%	91.0%	0.061	0.053	0.043	0.031	0.069	0.059	0.054	0.036
3	82.5%	85.3%	89.4%	90.8%	0.061	0.053	0.043	0.031	0.077	0.064	0.061	0.038
4	82.2%	85.0%	89.4%	91.0%	0.062	0.054	0.043	0.032	0.083	0.070	0.068	0.039
5	82.0%	85.1%	89.5%	90.9%	0.063	0.054	0.043	0.032	0.088	0.074	0.074	0.040
6	81.8%	85.1%	89.5%	90.7%	0.064	0.054	0.043	0.032	0.092	0.078	0.080	0.041
7	81.6%	85.1%	89.5%	90.6%	0.064	0.054	0.043	0.032	0.095	0.082	0.085	0.042
8	81.4%	85.0%	89.5%	90.6%	0.065	0.055	0.043	0.033	0.098	0.085	0.090	0.042
9	81.3%	85.0%	89.5%	90.5%	0.066	0.055	0.043	0.033	0.101	0.088	0.094	0.043
10	81.1%	84.6%	89.5%	90.5%	0.066	0.055	0.043	0.033	0.103	0.090	0.097	0.044
11	81.0%	84.6%	89.5%	90.4%	0.067	0.055	0.043	0.033	0.106	0.092	0.100	0.044
12	80.8%	84.6%	89.5%	90.5%	0.068	0.056	0.043	0.033	0.108	0.094	0.103	0.045
13	80.6%	84.4%	89.4%	90.4%	0.069	0.056	0.043	0.033	0.111	0.095	0.105	0.045
14	80.3%	84.3%	89.3%	90.4%	0.070	0.056	0.044	0.033	0.114	0.096	0.107	0.046
15	80.0%	84.3%	89.2%	90.4%	0.071	0.056	0.044	0.033	0.119	0.097	0.109	0.046
16	79.5%	84.3%	89.1%	90.3%	0.073	0.056	0.044	0.033	0.125	0.098	0.110	0.046

Table 5. **4D Shape Reconstruction for Unseen Motions (DFAUST)**. We evaluate IoU, Chamfer distance, and correspondence distance for 17 timeframes for the 4D shape reconstruction from sparse point cloud task on seen individuals but unseen motions of DFAUST [4] dataset.

Time step	IoU				Chamfer				Correspond.			
	OFlow	LPDC	CaDex	Ours	OFlow	LPDC	CaDex	Ours	OFlow	LPDC	CaDex	Ours
0	74.2%	76.8%	80.4%	84.5%	0.077	0.068	0.055	0.042	0.077	0.065	0.057	0.044
1	74.1%	76.8%	80.5%	84.5%	0.077	0.069	0.055	0.042	0.082	0.071	0.060	0.046
2	73.8%	76.7%	80.6%	84.5%	0.078	0.069	0.054	0.043	0.089	0.075	0.064	0.048
3	73.4%	76.5%	80.7%	84.4%	0.079	0.069	0.054	0.043	0.096	0.080	0.069	0.049
4	73.0%	76.5%	80.8%	84.4%	0.081	0.070	0.054	0.043	0.102	0.085	0.074	0.050
5	72.7%	76.6%	80.8%	84.3%	0.082	0.070	0.054	0.043	0.108	0.089	0.078	0.051
6	72.4%	76.3%	80.8%	84.2%	0.083	0.070	0.054	0.043	0.113	0.094	0.083	0.053
7	72.2%	76.2%	80.8%	84.1%	0.084	0.071	0.054	0.043	0.117	0.098	0.086	0.054
8	72.0%	76.0%	80.8%	84.1%	0.085	0.071	0.054	0.044	0.121	0.101	0.090	0.055
9	71.9%	76.1%	80.8%	84.0%	0.085	0.071	0.054	0.044	0.124	0.104	0.093	0.056
10	71.8%	76.1%	80.8%	84.0%	0.086	0.072	0.054	0.044	0.127	0.107	0.096	0.056
11	71.7%	75.9%	80.7%	83.9%	0.086	0.072	0.054	0.044	0.130	0.109	0.098	0.057
12	71.5%	75.9%	80.7%	84.0%	0.087	0.072	0.054	0.044	0.133	0.112	0.101	0.058
13	71.4%	75.8%	80.6%	83.9%	0.087	0.072	0.054	0.045	0.136	0.114	0.103	0.059
14	71.3%	75.7%	80.5%	83.7%	0.088	0.073	0.055	0.045	0.140	0.116	0.105	0.060
15	71.0%	75.6%	80.4%	83.7%	0.089	0.073	0.055	0.045	0.145	0.119	0.106	0.060
16	70.7%	75.7%	80.2%	83.7%	0.090	0.074	0.056	0.045	0.150	0.121	0.107	0.061

Table 6. **4D Shape Reconstruction for Unseen Individuals (DFAUST)**. We evaluate IoU, Chamfer distance, and correspondence distance for 17 timeframes for the 4D shape reconstruction from sparse point cloud task on unseen individuals of DFAUST [4] dataset.

Time step	IoU				Chamfer				Correspond.			
	OFlow	LPDC	CaDex	Ours	OFlow	LPDC	CaDex	Ours	OFlow	LPDC	CaDex	Ours
0	74.8%	63.3%	79.6%	89.6%	0.191	0.302	0.063	0.046	0.163	0.252	0.078	0.045
1	74.4%	62.6%	79.8%	89.6%	0.193	0.308	0.062	0.047	0.182	0.285	0.082	0.048
2	73.7%	62.3%	80.0%	89.4%	0.197	0.310	0.061	0.047	0.208	0.311	0.091	0.051
3	73.1%	62.0%	80.2%	89.3%	0.202	0.313	0.060	0.048	0.233	0.341	0.100	0.053
4	72.7%	61.6%	80.3%	89.2%	0.206	0.316	0.060	0.048	0.254	0.372	0.110	0.056
5	72.3%	61.3%	80.2%	89.1%	0.209	0.320	0.059	0.049	0.271	0.402	0.118	0.058
6	72.1%	61.0%	80.5%	88.9%	0.211	0.323	0.059	0.050	0.285	0.431	0.126	0.060
7	71.9%	60.6%	80.6%	88.9%	0.213	0.327	0.059	0.050	0.298	0.459	0.133	0.062
8	71.7%	60.3%	80.6%	88.7%	0.215	0.331	0.058	0.050	0.308	0.485	0.139	0.063
9	71.5%	59.9%	80.7%	88.6%	0.216	0.335	0.058	0.051	0.318	0.510	0.145	0.065
10	71.3%	59.6%	80.7%	88.6%	0.218	0.339	0.059	0.051	0.327	0.533	0.150	0.066
11	71.1%	59.2%	80.6%	88.6%	0.219	0.343	0.059	0.052	0.335	0.555	0.154	0.067
12	70.9%	58.9%	80.5%	88.5%	0.221	0.347	0.059	0.052	0.343	0.576	0.158	0.068
13	70.7%	58.6%	80.4%	88.5%	0.223	0.351	0.060	0.052	0.352	0.598	0.162	0.069
14	70.3%	58.2%	80.2%	88.4%	0.226	0.355	0.060	0.052	0.364	0.619	0.166	0.070
15	69.7%	57.9%	80.0%	88.4%	0.231	0.360	0.061	0.053	0.380	0.641	0.169	0.071
16	68.9%	57.6%	79.6%	88.3%	0.239	0.365	0.063	0.053	0.402	0.662	0.173	0.072

Table 7. **4D Shape Reconstruction for Unseen Motions (DT4D-A)** We evaluate IoU, Chamfer distance, and correspondence distance for 17 timeframes for the 4D shape reconstruction from sparse point cloud task on seen individuals but unseen motions of DT4D-A [29] dataset.

Time step	IoU				Chamfer				Correspond.			
	OFlow	LPDC	CaDex	Ours	OFlow	LPDC	CaDex	Ours	OFlow	LPDC	CaDex	Ours
0	62.4%	53.5%	64.2%	84.8%	0.294	0.404	0.129	0.056	0.216	0.296	0.150	0.057
1	62.1%	52.8%	64.4%	84.7%	0.296	0.412	0.128	0.056	0.235	0.330	0.157	0.060
2	61.7%	52.6%	64.5%	84.6%	0.300	0.414	0.127	0.056	0.260	0.358	0.169	0.062
3	61.4%	52.4%	64.6%	84.4%	0.304	0.417	0.127	0.057	0.283	0.390	0.183	0.065
4	61.1%	52.2%	64.6%	84.3%	0.307	0.420	0.126	0.057	0.303	0.422	0.197	0.068
5	60.9%	51.9%	64.7%	84.1%	0.309	0.423	0.126	0.057	0.321	0.453	0.211	0.070
6	60.7%	51.7%	64.8%	83.9%	0.311	0.427	0.126	0.058	0.336	0.483	0.224	0.072
7	60.5%	51.4%	64.8%	83.8%	0.313	0.430	0.125	0.058	0.350	0.511	0.235	0.074
8	60.4%	51.2%	64.8%	83.6%	0.315	0.433	0.125	0.059	0.362	0.538	0.246	0.076
9	60.2%	51.0%	64.8%	83.4%	0.317	0.437	0.125	0.059	0.374	0.563	0.256	0.077
10	60.1%	50.7%	64.8%	83.3%	0.319	0.440	0.125	0.059	0.385	0.588	0.266	0.078
11	60.0%	50.5%	64.8%	83.3%	0.321	0.443	0.125	0.059	0.395	0.611	0.274	0.080
12	59.8%	50.3%	64.8%	83.2%	0.323	0.446	0.125	0.060	0.405	0.633	0.282	0.081
13	59.7%	50.1%	64.7%	83.1%	0.325	0.449	0.126	0.060	0.416	0.654	0.289	0.082
14	59.4%	49.9%	64.6%	83.0%	0.329	0.452	0.126	0.060	0.428	0.675	0.296	0.083
15	59.1%	49.7%	64.5%	82.9%	0.334	0.455	0.127	0.060	0.445	0.696	0.303	0.084
16	58.6%	49.5%	64.3%	82.8%	0.340	0.459	0.128	0.061	0.466	0.716	0.309	0.085

Table 8. **4D Shape Reconstruction for Unseen Individuals (DT4D-A)** We evaluate IoU, Chamfer distance, and correspondence distance for 17 timeframes for the 4D shape reconstruction from sparse point cloud task on unseen individuals of DT4D-A [29] dataset.

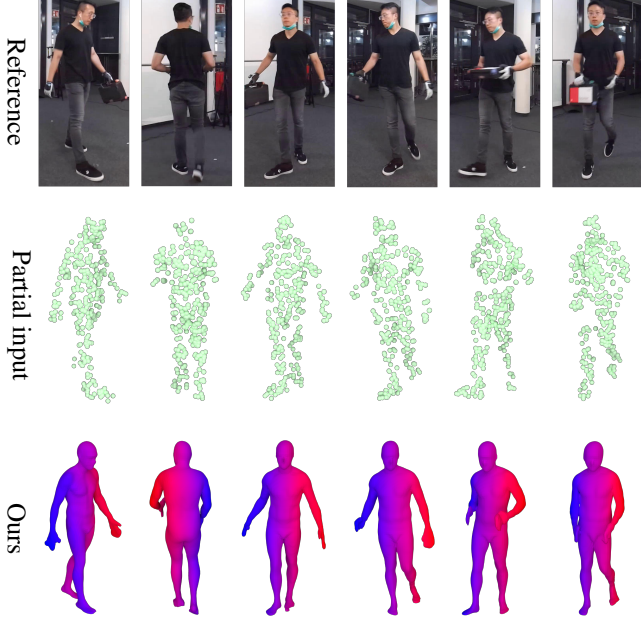


Figure 11. **4D Shape Completion.** on the BEHAVE dataset [2]. The input, consisting of 300 points, is sub-sampled from a point cloud back-projected from the depth frame. Our approach successfully recovers accurate 4D human motion captured in real-world scenarios, showcasing its generalization ability to real data.

D.2. 4D Shape Completion

In the more challenging task of 4D shape completion from partial point clouds, our model shows noticeable improvements over existing state-of-the-art methods. The quantitative results, as illustrated in Fig. 14 and Fig. 15, demonstrate substantial performance enhancements, with a lower error rate in scenarios involving unseen motions and individuals. This underscores the robustness of our approach.

Our model’s capabilities are especially evident in the D-FAUST dataset [4], achieving more accurate reconstructions of complex human body parts, like hands and feet. These parts, typically difficult to reconstruct, are rendered with higher fidelity. Furthermore, the DT4D-A dataset [29], known for its varied topologies, shows our model’s strengths. In this dataset, our model not only demonstrates lower reconstruction errors for animal shapes but also captures their motion with greater accuracy. This performance, across a diverse range of topologies, highlights the adaptability and effectiveness of our model in complex 4D shape reconstruction tasks.

E. Real-world Data Test

In this section, we validate our model using data from the real-world BEHAVE dataset [2], employing four Kinect RGB-D cameras to capture RGB color and depth frames. In our case, we utilize a single view from a fixed camera to

align with our previous partial scan setting. Similarly, the depth map is back-projected into a 3D point cloud, serving as a partial input for our model. In Fig. 11, we present a visual representation of our reconstruction process with the corresponding input and reference RGB frame.

The results demonstrate the robustness of our model in scenarios characterized by markedly incomplete scans, such as instances where limbs, like the leg or arm, are obscured by structures such as a grasped object in the hand. This resilience stems from the inherent capabilities of the diffusion model, empowering our model to infer potential structures even in the presence of significant occlusions. This effectiveness is attributed to the learned latent distribution, highlighting the model’s capacity to generalize and extrapolate beyond the limitations imposed by incomplete or obstructed input scans.

Notably, our method exhibits remarkable reliability even without the need for model fine-tuning on the real dataset. This stability is particularly evident when addressing inherent noise present in sensor captures, further affirming the efficacy of our approach in handling challenging real-world scenarios.

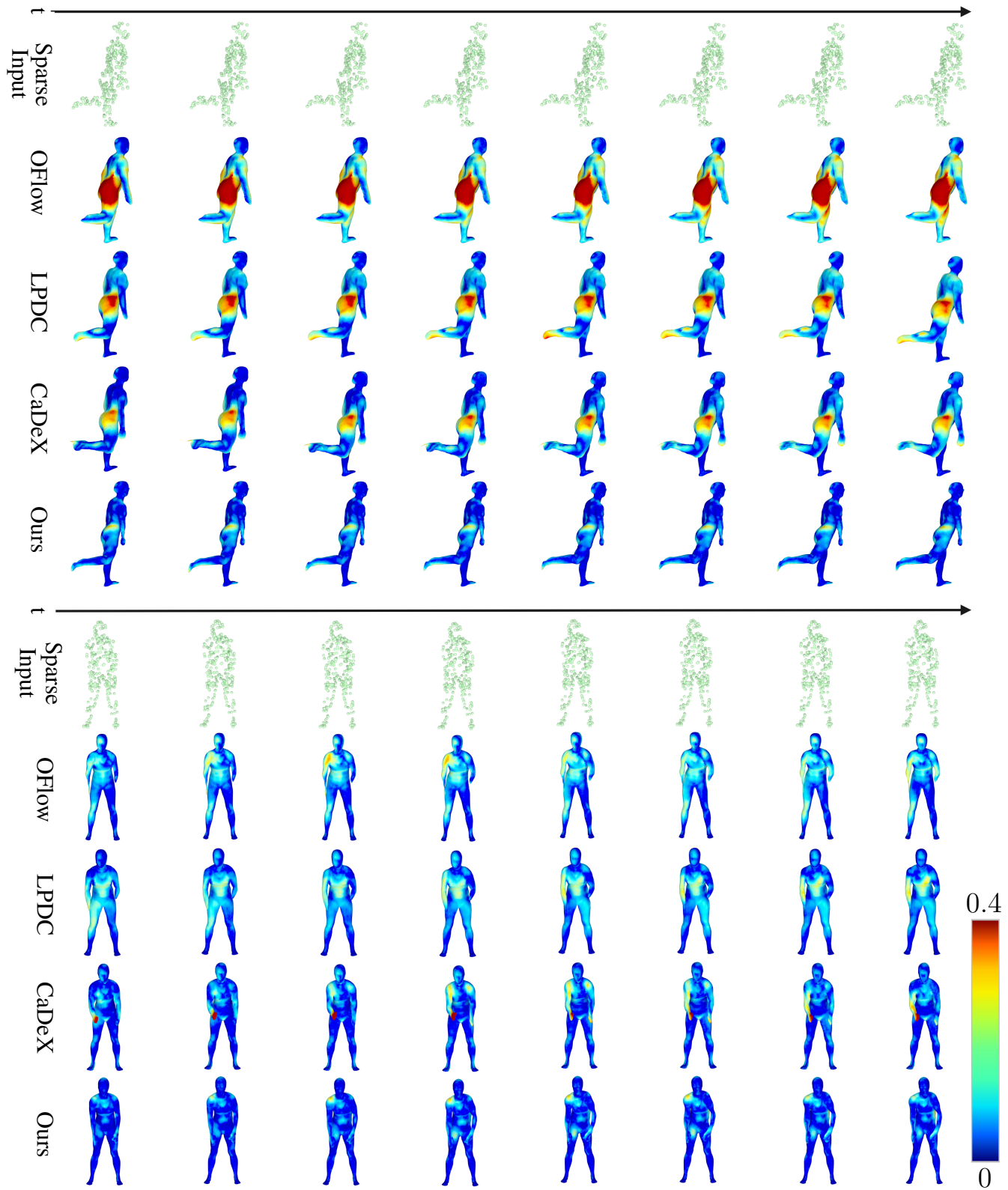


Figure 12. **4D Shape Reconstruction from sparse and noisy point clouds on the D-FAUST[4] dataset.** One for unseen motion (upper) and another for unseen individuals (lower).

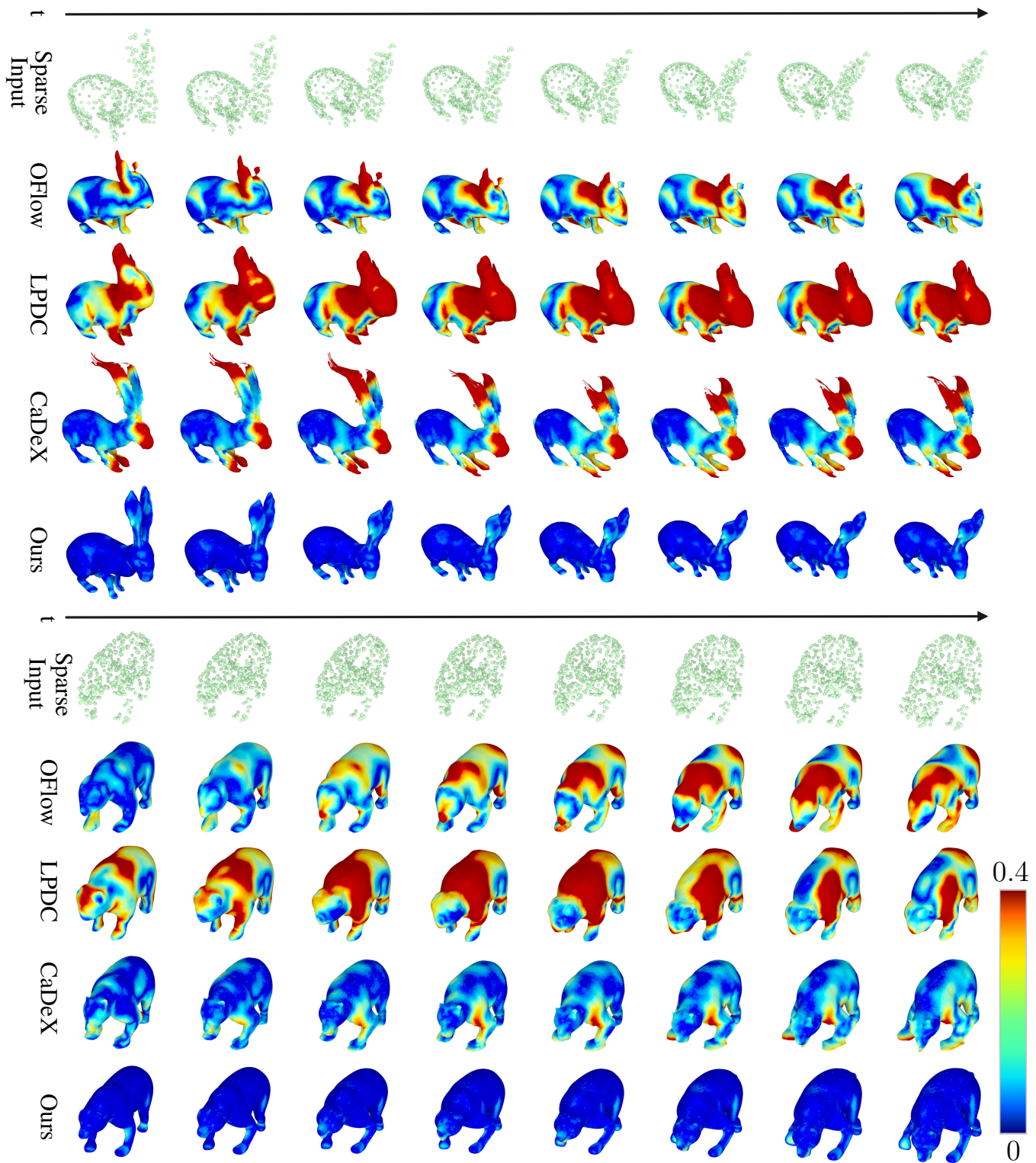


Figure 13. **4D Shape Reconstruction from sparse and noisy point clouds on the DT4D-A [29] dataset.** One for unseen motion (upper) and another for unseen individuals (lower).

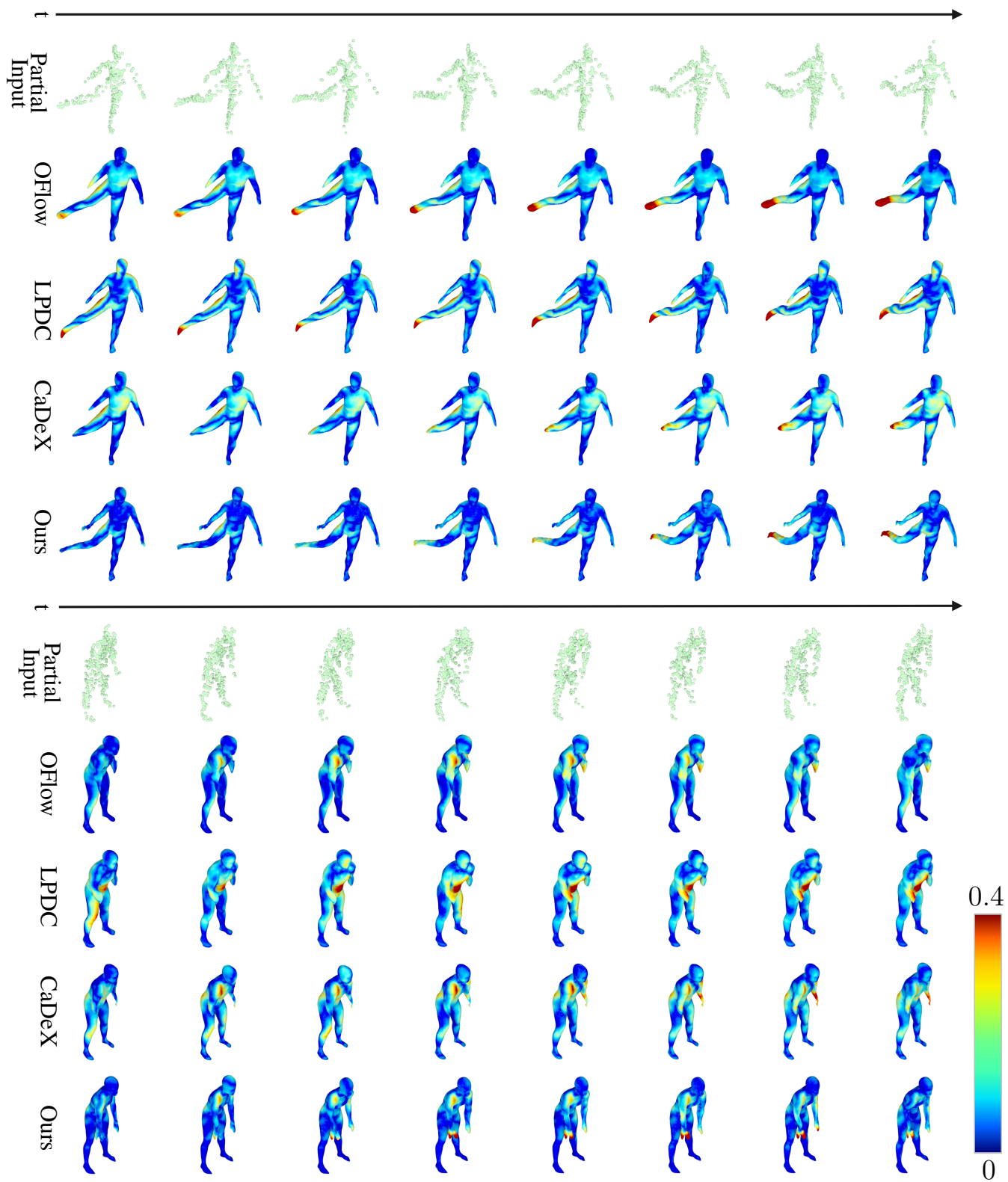


Figure 14. **4D Shape Completion from partial point clouds on the D-FAUST[4] dataset.** One for unseen motion (upper) and another for unseen individuals (lower).

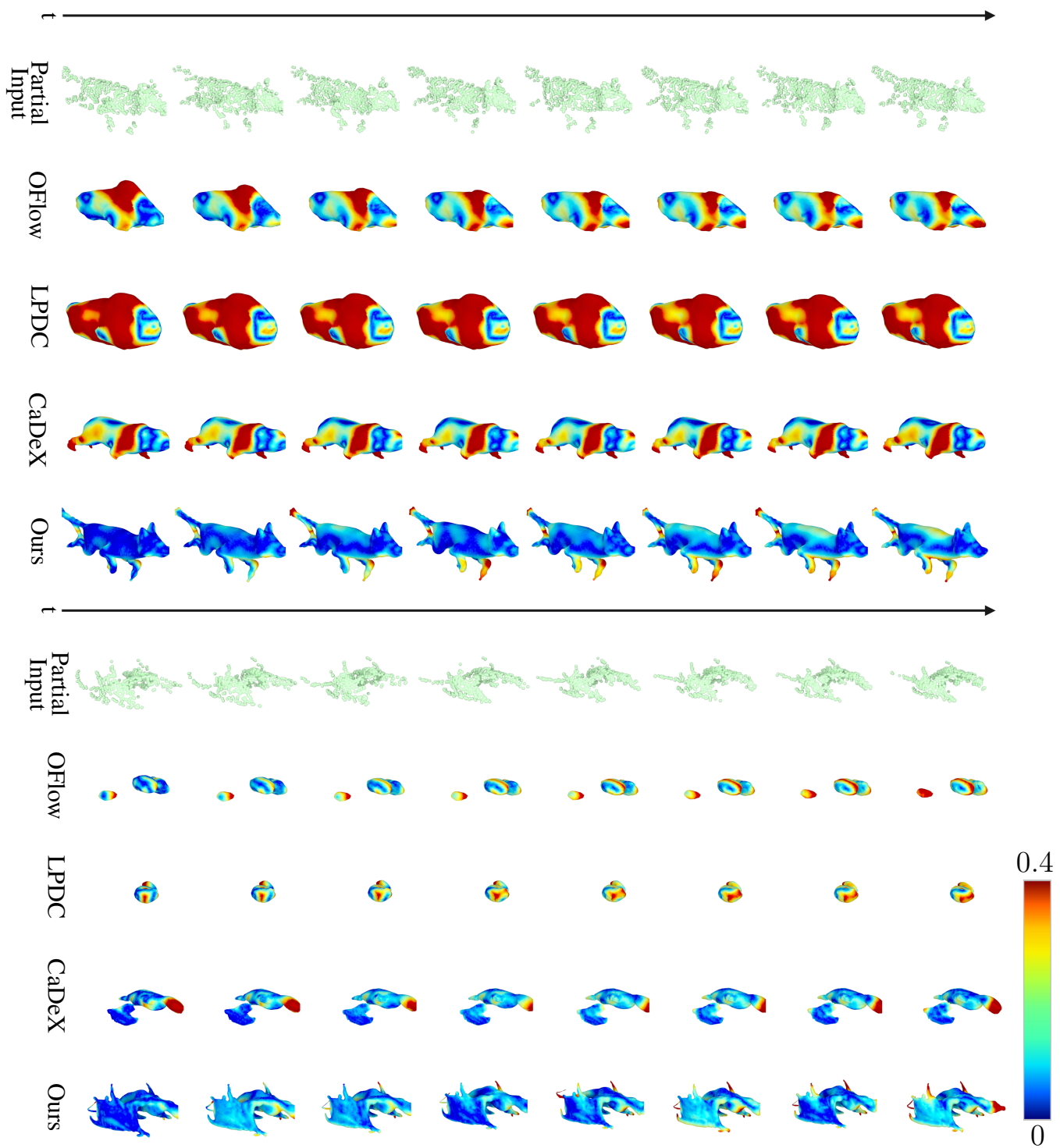


Figure 15. **4D Shape Completion from partial point clouds on the DT4D-A [29] dataset.** One for unseen motion (upper) and another for unseen individuals (lower).